

NASA/CR-97- 206647

INTERIM
IN-43-CR
1998
044 463

SEMI-ANNUAL REPORT

(for July - December 1997)

Contract Number NAS5-31363

OCEAN OBSERVATIONS WITH EOS/MODIS:

Algorithm Development and Post Launch Studies

Howard R. Gordon
University of Miami
Department of Physics
Coral Gables, FL 33124

(Submitted January 1, 1998)

Semi-Annual Report (1 July – 31 December 1997) NAS5-31363

Preamble

As in earlier reports, we will continue to break our effort into six distinct units:

- Atmospheric Correction Algorithm Development
- Whitecap Correction Algorithm
- In-water Radiance Distribution
- Residual Instrument Polarization
- Pre-launch/Post-launch Atmospheric Correction Validation
- Detached Coccolith Algorithm and Post-launch Studies

This separation has been logical thus far; however, as launch of AM-1 approaches, it must be recognized that many of these activities will shift emphasis from algorithm development to validation. For example, the second, third, and fifth bullets will become almost totally validation-focussed activities in the post-launch era, providing the core of our experimental validation effort. Work under the first bullet will continue into the post-launch time frame, but will be driven in part by algorithm deficiencies revealed as a result of validation activities. We will continue to use this format for CY98.

Abstract

Significant accomplishments made during the present reporting period:

- We expanded our “spectral-matching” algorithm (SMA), for identifying the presence of absorbing aerosols and simultaneously performing atmospheric correction and derivation of the ocean’s bio-optical parameters, to the point where it could be added as a subroutine to the MODIS water-leaving radiance algorithm.
- A modification to the SMA that does not require detailed aerosol models has been developed. This is important as the requirement for realistic aerosol models has been a weakness of the SMA.
- We successfully acquired micro pulse lidar data in a Saharan dust outbreak during ACE-2 in the Canary Islands.

1. Atmospheric Correction Algorithm Development.

a. Task Objectives:

During CY 1997 there were seven objectives under this task. Task (i) below was considered to be the most critical. If the work planned under this task was successful, a module that enables the algorithm to distinguish between weakly- and strongly-absorbing aerosols would be included in the atmospheric correction algorithm. The seven tasks are listed below.

(i) We will continue the study of the “spectral-matching” algorithm with the goal of having an algorithm ready for implementation by the end of CY 1997.

(ii) We need to test the basic atmospheric correction algorithm with actual ocean color imagery. We will do this by looking at SeaWiFS and OCTS imagery as they become available.

(iii) We must implement our strategy for adding the cirrus cloud correction into the existing atmospheric correction algorithm. Specific issues include (1) the phase function to be used for the cirrus clouds, (2) the details of making two passes through the correction algorithm, and (3) preparation of the required look up tables (LUTs).

(vi) The basic correction algorithm yields the product of the diffuse transmittance and the water-leaving reflectance. However, we have shown that the transmittance depends on the angular distribution of the reflectance only when the pigment concentration is very low and then only in the blue. We need to develop a method to include the effects of the subsurface BRDF for low-pigment waters in the blue.

(v) We will initiate a study to determine the efficacy of the present atmospheric correction algorithm on removal for the aerosol effect from the measurement of the fluorescence line height (MOD 20).

(vi) We will examine methods for efficiently including earth-curvature effects into the atmospheric correction algorithm. This will most likely be a modification of the look-up tables for the top-of-the-atmosphere contribution from Rayleigh scattering.

(vii) We will examine the necessity of implementing our out-of-band correction to MODIS.

b. Work Accomplished:

(i) We considered this task to be our most important atmospheric correction activity of 1997, and as such the major part of our effort on atmospheric correction was focussed on it. During this CY, we have further tested our spectral-matching algorithm (SMA) that, although very slow, is capable of distinguishing between weakly- and strongly-absorbing aerosols. It is based on combining a model of the atmosphere with a water-leaving radiance model for the ocean, and effecting a variation of the relevant parameters until a satisfactory fit to the MODIS top-of-atmosphere radiance is achieved. In simulations it showed significant success in detecting the absorption properties of the aerosol, i.e., distinguishing between weakly- and strongly-absorbing aerosols. We found ways to significantly increase the speed of the algorithm, and to enable it to operate using the same set of lookup tables that the basic algorithm uses. This enabled us to incorporate it in the basic correction algorithm, to be called each $N \times N$ pixels (where $N \sim 10 - 100$). In our present implementation the SMA simply returns a flag indicating the possible presence of absorbing aerosols. In subsequent implementations, we will return the oceanic and atmospheric properties. Unfortunately, at present we are not confident that models of absorbing aerosols, e.g., wind-blown dust, are sufficiently accurate to be effective candidate aerosol models, and this is impeding the full implementation.

As with our original algorithm, the SMA requires candidate aerosol models, so it is important to understand the extent to which the candidate aerosol models need to be realistic. To try to understand this, we have revised the SMA by replacing the Shettle and Fenn aerosol models with Junge power-law models with a size-independent refractive index. This is an enormous simplification. We also replaced our “brute-force” search with a nonlinear optimization with which the aerosol size distribution, aerosol refractive index, and ocean properties are determined. Simulations show that excellent retrievals of the ocean’s pigment concentration are obtained; however, the price is a loss of accuracy in the estimate of the aerosol optical depth. A detailed report describing these results is presented as an appendix to this report.

We have also expended much effort toward increasing the speed of the present MODIS algorithm. Significant gains have been achieved by not computing everything at each pixel. Rather, the LUT values that are found for a given pixel are retained for 5-10 pixels. Although there is a small loss in accuracy, the increase in speed justifies it. This speed increase is an important, because the spectral-matching algorithm is very slow.

(ii) Some imagery has been acquired from SeaWiFS. We have prepared a set of SeaWiFS-specific LUTs that will enable processing SeaWiFS imagery using the present MODIS code. This will allow a preliminary validation of the code.

Semi-Annual Report (1 July – 31 December 1997) NAS5-31363

(iii) None. In the light of the success of our spectral-matching algorithm, we may have to make significant modifications in our original strategy. This task has been put on hold to free resources for examination of task (i). The issues will be addressed during CY 1998 with the goal of having a complete implementation strategy ready during CY 1998.

(iv) No work was carried out on this task.

(v) No work was carried out on this task.

(vi) No work was carried out on this task.

(vii) The specifics of incorporating the out-of-band corrections in the MODIS algorithm have been worked out.

c. Data/Analysis/Interpretation: See item b above.

d. Anticipated Future Actions:

(i) We will continue work on the spectral-matching algorithm. Of particular interest is to implement the SMA optimization described in the Appendix. We will implement this method and test its efficacy with SeaWiFS imagery. We will examine the necessity of including bidirectional effects into the ocean model portion of the SMA.

(ii) We shall continue testing the algorithm with SeaWiFS imagery through the first 7-9 months of CY 98, at which time we will switch to actual MODIS imagery. In particular, as described in (i), we want to test the SMA with real ocean color data.

(iii) The cirrus cloud issue in the presence of our spectral-matching method needs to be explored. We will resolve the spectral-matching questions first, then devise a strategy to implement the cirrus correction.

(iv) An ocean BRDF model will be developed in conjunction with the SMA (i), and validation (see 5 below).

(v) We will perform a basic test of the efficacy of the correction algorithm for retrieving the fluorescence line height.

(vi) None.

(vii) None, until we are provided with the final MODIS spectral response functions.

f. Publications:

H.R. Gordon, T. Zhang, F. He, and K. Ding, Effects of stratospheric aerosols and thin cirrus clouds on atmospheric correction of ocean color imagery: Simulations, *Applied Optics*, **36**, 682–697 (1997).

H.R. Gordon, Atmospheric Correction of Ocean Color Imagery in the Earth Observing System Era, *Jour. Geophys. Res.*, **102D**, 17081–17106 (1997).

H. Yang and H.R. Gordon, Remote sensing of ocean color: Assessment of the water-leaving radiance bidirectional effects on the atmospheric diffuse transmittance, *Applied Optics*, **36**, 7887–7897 (1997).

H.R. Gordon, T. Du, and T. Zhang, Remote sensing ocean color and aerosol properties: resolving the issue of aerosol absorption, *Applied Optics*, **36**, 8670–8684 (1997).

2. Whitecap Correction Algorithm (with K.J. Voss).

We believed that the basic objectives of this task had been realized, work was suspended until the validation phase, except insofar as the radiometer would be operated at sea when sufficient number of personnel were available. Our goal was to retain experience in operating and maintaining the instrumentation in preparation for the validation phase of the contract. However, by virtue of the surprisingly low reflectance increase due to whitecaps that we measured in the Tropical Pacific, we decided in July to reanalyze the data. This is a unique data set (our most important), as it was acquired in the trade winds with moderately high winds (8-12 m/s) and practically unlimited fetch and duration.

a. Task Objectives:

Operate the radiometer at sea to maintain experience in preparation for the validation phase and reanalyze the Tropical Pacific data.

b. Work Accomplished:

An undergraduate was hired part time and has learned to analyze the data. He is developing a differential filter to distinguish background from whitecaps, automatically. This is very tedious as it requires comparing the radiometer with the video monitor on a sample-to-sample basis.

c. Data/Analysis/Interpretation

At this time we have reduced the calibration data for the February cruise, but not the whitecap data.

d. Anticipated Future Actions:

First, we will reanalyze the Tropical Pacific whitecap data, then the data acquired during the February cruise. Second, we will operate the radiometer on the SeaWiFS initialization cruise in February 1998. This cruise will serve as a test bed for our initialization cruise for MODIS in October.

e. Problems/Corrective Actions: None

f. Publications:

K.D. Moore, K.J. Voss, and H.R. Gordon, Spectral reflectance of whitecaps: Instrumentation, calibration, and performance in coastal waters, *Jour. Atmos. Ocean. Tech.* (In Press).

3. In-water Radiance Distribution (with K.J. Voss).

a. Task Objectives:

The main objective in this task is to obtain upwelling radiance distribution data at sea for a variety of solar zenith angles to understand how the water-leaving radiance varies with viewing angle and sun angle.

b. Work accomplished:

Data was acquired during the July 1997 cruise with this instrument. We have reduced this data to radiometric quantities and are now working with the data. During this cruise we had an opportunity to take an extensive data set during one afternoon (July 23), in which data was acquired with sun angles varying from approximately 40 degrees to 85 degrees. This will give us a good data set to evaluate the effect of sun angle on the upwelling radiance distribution at the MOBY site.

c. Data/Analysis/Interpretation:

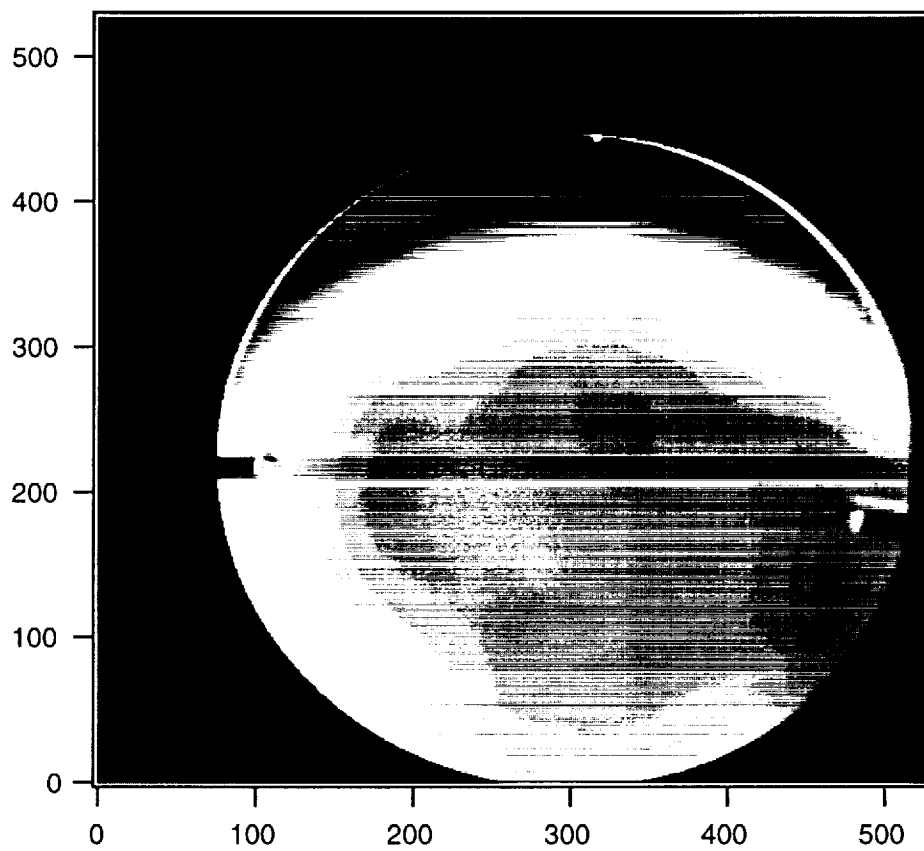
We have been concentrating our data analysis efforts on the extensive data set taken on July 23. As an example, we show a polar-coordinate image of the upwelling radiance distribution at 560 nm and a solar zenith angle of 66 degrees in the figure on the following page. Radiance increases from the red colors to the blue colors (blue highest). The colors are arranged linearly. This figure illustrates that the radiance distribution is neither uniform nor symmetric near the surface (the measurement depth was 2 meters). We are concentrating with our analysis on several "cuts" through this data at 4 azimuthal angles. We will be comparing these images with results from a Monte Carlo model to test how well we can model these factors. In addition we will be comparing our measurements with the f/Q model of Morel (which is being used in other models in the community).

d. Anticipated future actions:

We will be continuing our data analysis. In addition we are calibrating the instrument and will be participating in another cruise with Dennis Clark in Hawaii during January and February of 1998, as well as the MODIS initialization cruise in October.

e. Problems/Corrective actions: None.

f. Publications: None.



4. Residual Instrument Polarization.

The basic question here is: if the MODIS responds to the state of polarization state of the incident radiance, given the polarization-sensitivity characteristics of the sensor, how much will this degrade the performance of the algorithm for atmospheric correction, and how can we correct for these effects?

a. Task Objectives:

Add a module to perform the correction for residual instrument polarization.

b. Work Accomplished:

A module was added to perform the correction for residual instrument polarization.

c. Data/Analysis/Interpretation: None.

d. Anticipated Future Actions:

Although this task is now basically complete. All that remains is incorporating the SBRS/MCST polarization-sensitivity data into the module.

e. Problems/Corrective Actions: None

f. Publications:

H.R. Gordon, T. Du, and T. Zhang, Atmospheric Correction of Ocean Color Sensors: Analysis of the Effects of Residual Instrument Polarization Sensitivity, *Applied Optics*, **36**, 6938-6948 (1997).

5. Pre-launch/Post-launch Atmospheric Correction Validation (with K.J. Voss).

a. Task Objectives:

The long-term objectives of this task are four-fold:

(i) First, we need to study aerosol optical properties over the ocean in order to verify the applicability of the aerosol models used in the atmospheric correction algorithm. Effecting this requires obtaining long-term time series in typical maritime environments. This will be achieved using a CIMEL sun/sky radiometer that can be operated in a remote environment and send data back to the laboratory via a satellite link. These are similar the radiometers used by B. Holben in the AERONET Network.

(ii) Second, we must be able to measure the aerosol optical properties from a ship during the initialization/calibration/validation cruises. The CIMEL-type instrumentation cannot be used (due to the motion of the ship) for this purpose. The required instrumentation consists of an all-sky camera (which can measure the entire sky radiance, with the exception of the solar aureole region) from a moving ship, an aureole camera (specifically designed for ship use) and a hand-held sun photometer. We had a suitable sky camera and sun photometer but had to construct an aureole camera. Our objective for this calendar year was to make measurements at sea with this instrumentation, both to collect a varied data set and to test the instrumentation and data reduction procedures.

In the case of strongly-absorbing aerosols, we have shown that knowledge of the aerosol vertical structure is critical. Thus, we need to be able to measure the vertical distribution of aerosols during validation exercises as well as build a climatology of the vertical distribution of absorbing aerosols. This will be accomplished with ship-borne LIDAR. We have procured a LIDAR system and modified it for ship operations.

(iii) The third objective is to determine how accurately the radiance at the top of the atmosphere can be determined based on measurements of sky radiance and aerosol optical thickness at the sea surface. This requires a critical examination of the effect of radiative transfer on "vicarious" calibration exercises.

(iv) The forth objective is to utilize data from other sensors that have achieved orbit (OCTS, POLDER, MSX), or are expected to achieve orbit (SeaWiFS) prior to the launch of MODIS, to validate and fine-tune the correction algorithm.

b. Work Accomplished:

(i) The CIMEL was reinstalled during July in the Dry Tortugas and worked well for 2 months before failing in late September. We went down to remove it and send it back to Goddard for recalibration and found that it had fallen over (some bolts had been removed or not installed properly). The instrument was recalibrated and repaired at Goddard and we have reinstalled it in the Dry Tortugas (as of mid December). There were some problems during the recalibration, a filter was replaced and the tracking repaired, so the recalibration took longer than expected. We are investigating getting another CIMEL from the SeaWiFS instrument pool in the future. This will be used to swap out with our instrument during recalibration in the future, reducing downtime. In addition we are working on installing the Demonstrat program, which is used to view the data products, on one of our computers to allow easier access to the data.

(ii) Aureole and sky camera data acquired during the July cruise was reduced during this period. These data were analyzed, specifically for several locations while the cruise went near the volcanic plume to look at the retrieved size distribution of particulates in the plume.

The micro-pulse lidar system (MPL) was deployed in Tenerife, Canary Islands during June and July of 1997 in support of the Aerosol Characterization Experiment 2 (ACE-2). The primary goal of ACE-2 was to assess the radiative forcing due to anthropogenic aerosols over the North Atlantic. In addition, it was also possible to analyze the radiative impact of desert dust aerosols from North Africa. The primary purpose of operating the MPL during ACE-2 was to acquire information about the vertical structure of the dust layers. The second purpose for the ACE-2 MPL deployment was to perform calibration procedures that are not possible in Miami and to test the MPL and planned lidar analysis algorithms for future MPL operations. Prior to the official start of ACE-2, an additional duty was assigned to the MPL operator by ACE-2 Headquarters. This consisted of faxing morning "real-time" lidar data, with initial estimates of the vertical location of any aerosol layers, to ACE-2 Headquarters for the morning preflight briefing of the ONR CIRPAS Aircraft Pelican crew. The morning lidar data was used by the Pelican crew to aid in planning their flight paths.

The MPL was shipped to Tenerife in May 1997 and was installed at Tenerife's Observatorio de Izana (IZO) which is located on a mountain ridge near the center of the island at an altitude of 2367 m above sea level. The location and altitude of IZO made it possible to perform both calibration procedures and study the vertical structure of dust layers moving west off the coast of Africa. The MPL was installed and began operational testing on June 14, 1997. Regular ACE-2 operation began on June 18, 1997. Regular MPL ACE-2 operation consisted of vertical, horizontal, and slant path (lidar tilted to a zenith angle of 60 degrees) measurements at specified times of each day. Slant

Semi-Annual Report (1 July – 31 December 1997) NAS5–31363

path measurements were made during midday to avoid direct sunlight from entering the detector and causing possible damage to the instrument. Vertical and horizontal measurements were made to study the vertical and horizontal structure of any aerosol layers and to perform calibration procedures. In addition, vertical measurements from 1000 GMT were used for the Pelican preflight planing sessions. Regular MPL ACE-2 operation continued until shutdown on June 25, 1997. The MPL was then shipped back to Miami.

(iii) The theoretical aspects of this work have been completed. The next phase is to use surface measurements to predict top-of-atmosphere radiance.

(iv) We have prepared a duplicate version of the MODIS algorithm code to use the SeaWiFS spectral bands. This will be used to test the MODIS code with SeaWiFS data.

c. Data/Analysis/Interpretation:

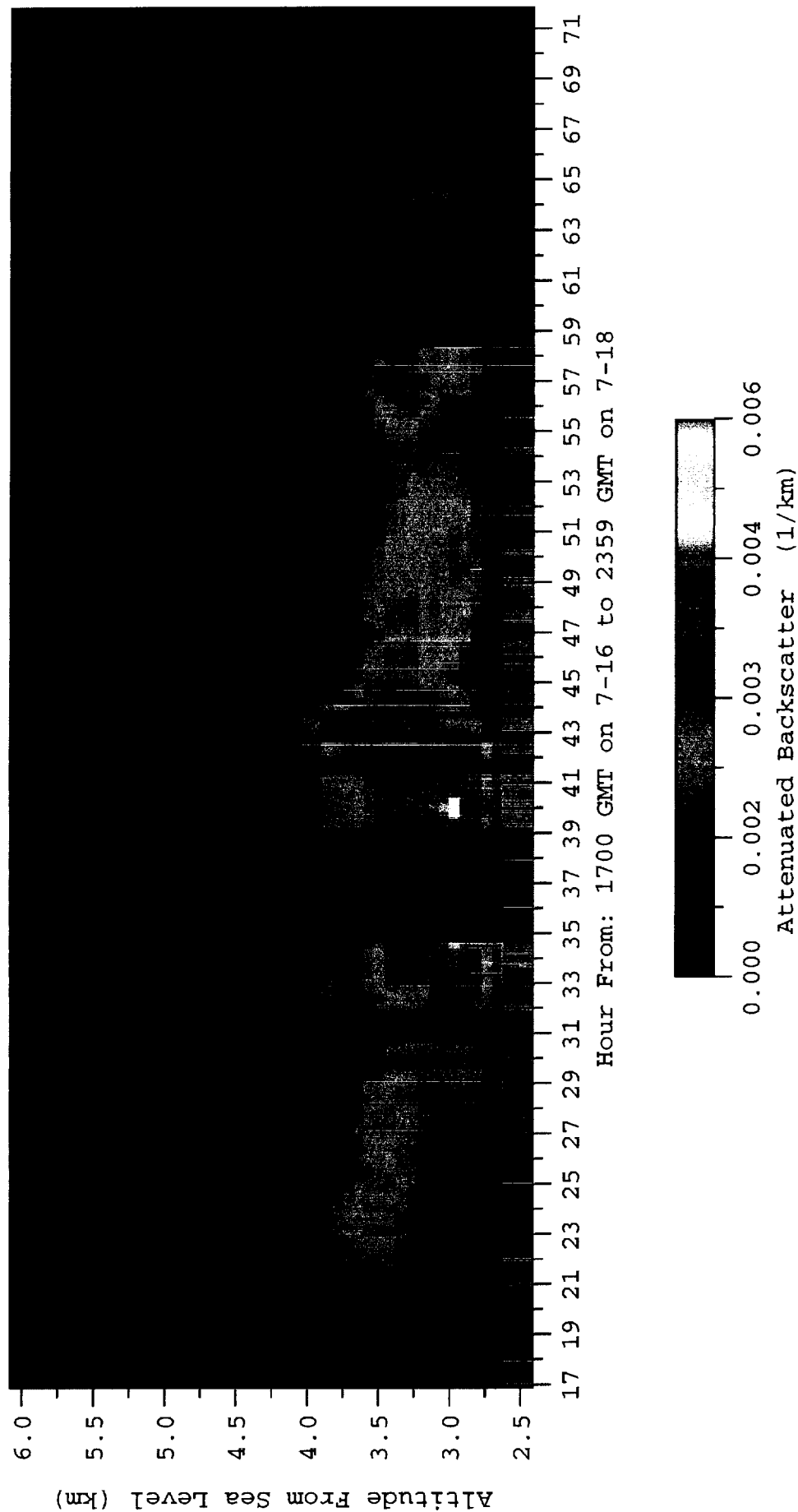
(ii) Two instrument problems occurred with the MPL during ACE-2. The first problem was due to a poor cable connection from the lidar receiver to the MPL scalar unit. Normal nighttime temperatures at IZO during June were around 10°C. Contraction of the BNC cable connector due to the cold weather resulted in the loss of nighttime data from June 18 to June 27, 1997. This problem was fixed by changing cables on June 28, 1997. The second MPL problem to occur during ACE-2 was attributed to the MPL laser. The laser doubling crystal burned midway through ACE-2 due to a poor ground connection to the laser temperature controller. This resulted in distortion of the outgoing laser pulses and a gradually decreasing signal-to-noise ratio throughout the month of July. It was not possible to perform normal MPL calibration procedures for the ACE-2 MPL data because of the laser problem. A modified calibration procedure was developed which normalized the lidar signals to a Rayleigh only lidar signal using MPL data from clean nighttime periods. This modified calibration procedure was used to correct all the ACE-2 MPL data.

The initial results using the modified calibration procedure are very promising. In particular, the day of July 17, 1997 has been analyzed to study the validity of the calibrations. There were three significant dust events during ACE-2, the second occurred during the period July 16 – July 18, 1997. The figure on the following page shows a time series plot of attenuated backscatter measured with the MPL during this dust event. The range-corrected lidar signal is defined as:

$$S(z) = CE[\beta_R(z) + \beta_A(z)] \exp[-2[\tau_R(z) + \tau_A(z)]],$$

where z is the range (km), C is the instrument constant, E is the output energy, $\beta(z)$ is the backscatter coeff. (1/km), and $\tau(z)$ is the optical depth. The subscripts R and A denote Rayleigh and Aerosol respectively. Attenuated backscatter is defined as $S(z)/CE$. It is the total backscatter

Figure 1: Attenuated Backscatter Coeff. (July 16 - July 18)



Semi-Annual Report (1 July – 31 December 1997) NAS5-31363

coefficient times the transmission squared. This quantity is not dependent on an inversion algorithm and is the initial data product from the MPL. The figure shows the beginning of the dust event (approximately 2100 GMT on July 16, 1997) as well as the vertical structure of the layer until its disappearance during the evening of July 18, 1997. Gaps in the figure are due to periods where the MPL was performing horizontal or slant path measurements. Horizontal and slant path ACE-2 data have not yet been analyzed.

On July 17, 1997 at 1830 GMT, simultaneous measurements of the aerosol optical depth (AOD) were made at IZO by a NASA AERONET Cimel sunphotometer¹, as well as on top of Teide (Tenerife's volcano, altitude 3500 m) with a YES shadowband², and by the Pelican's suntracking sunphotometer³ as the aircraft spiraled down above IZO from an altitude of approximately 3800 m. Recent comparisons of the MPL AOD vertical profile with the AOD profile of from Pelican and the AOD from Teide show very good agreement (within 0.03 AOD units at all altitudes from 2367 m to 3800 m). The AOD from the IZO Cimel was used as an input constraint in the MPL inversion algorithm and thus was not part of the lidar comparison, however, comparison of the IZO Cimel AOD with the Pelican AOD at 2367 m agree within about 0.01 AOD units. The good agreement between the MPL AOD profiles and those of independent instruments, as well as analysis of corrected clean nighttime lidar data (inversions of corrected data do show clean, insignificant aerosol amounts) show that the modified correction procedure has been a success.

d. Anticipated Future Actions:

(i) The CIMEL is reinstalled in the Dry Tortugas, and we are looking forward to collecting coincident data from the CIMEL and SeaWiFS satellite. In particular we would like to see data like this after a winter cold front, when the atmosphere is typically clearer than normal.

(ii) The aureole and sky camera are being recalibrated in anticipation of another cruise in January-February. We will also continue with the data reduction for these instruments.

Future use of the ACE-2 MPL data is currently being planned. The data will be made directly available to all ACE-2 participants as outlined in the ACE-2 guidelines. The data will also be the focus of at least two planned papers. The first will describe the MPL ACE-2 system and the problems and resulting calibration procedures used to correct the data. The second paper will involve other ACE-2 participants and will focus on closure analysis of the type described above for the day of July 17, 1997. The comparison of lidar derived aerosol optical properties, such as the

¹ B. Holben, A. Smirnov (personal communication)

² P. Formenti, M. Andreae (personal communication)

³ B. Schmid, P. Russell, J. Livingston, P. Durkee (personal communication)

Semi-Annual Report (1 July – 31 December 1997) NAS5-31363

extinction coefficient and the AOD, with those of other independent instruments in the near-range lidar field (the lidar range most effected by lidar overlap and afterpulse problems, 0–5 km) is a novel and important comparison in the field of lidar research. The initial agreement between the MPL AOD and the other instruments (within 0.03 AOD units) demonstrates the possibility of using MPL data to acquire accurate aerosol vertical profiles. In addition to the two planned ACE-2 papers, the ACE-2 MPL data will be a primary portion of the dissertation of graduate student E.J. Welton.

The MPL has been repaired and returned to Miami. We will deploy it during the January-February SeaWiFS initialization cruise and the October-November MODIS initialization cruise.

e. Problems/corrective actions: None.

f. Publications:

T. Zhang and H.R. Gordon, Columnar aerosol properties over oceans by combining surface and aircraft measurements: sensitivity analysis, *Applied Optics*, **36**, 2650–2662 (1997).

T. Zhang and H.R. Gordon, Retrieval of elements of the columnar aerosol scattering phase matrix from sky radiance over the ocean: simulations, *Applied Optics*, **36**, 7948–7959 (1997).

D.K. Clark, H.R. Gordon, K.J. Voss, Y. Ge, W. Broenkow, and C. Trees, Validation of Atmospheric Correction over the Oceans, *Jour. Geophys. Res.*, **102D** 17209–17217 (1997).

K.J. Voss and Y. Liu, Polarized radiance distribution measurements of skylight: Part 1, system description and characterization, *Applied Optics* **36**, 6083–6094 (1997).

Y. Liu and K.J. Voss, Polarized radiance distribution measurements of skylight: Part 2, experiment and data, *Applied Optics* **36**, 8753–8764 (1997).

H. Yang and H.R. Gordon, Retrieval of the Columnar Aerosol Phase Function and Single Scattering Albedo from Sky Radiance over Land: Simulations, *Applied Optics* (Accepted).

H.R. Gordon, In-orbit calibration strategy of ocean color sensors, *Remote Sensing of Environment* (Accepted).

6. Detached Coccolith Algorithm and Post Launch Studies (W.M. Balch).

a. Task Objectives:

Our MODIS work during involves understanding all aspects of the influence of suspended calcium carbonate particles on inherent optical properties in the sea. Work during this reporting period focused on several areas: processing cell count, atomic absorption, particulate organic carbon, and scattering data from MODIS pre-launch cruises in the Gulf of Maine, preparation and submission of three MODIS-related manuscripts, another MODIS pre-launch cruise to the Gulf of Maine to examine in situ properties of calcite particles, and analysis calcite optical properties from the Arabian Sea.

The algorithm for retrieval of the detached coccolith concentration from the coccolithophorid, *E. huxleyi* is described in detail in our ATBD. The key is quantification of the backscattering coefficient of the detached coccoliths. Our earlier studies focused on laboratory cultures to understand factors affecting the calcite-specific backscattering coefficient. A thorough understanding of the relationship between calcite abundance and light scattering, in situ, will provide the basis for a generic suspended calcite algorithm. As with algorithms for chlorophyll, and primary productivity, the natural variance between growth related parameters and optical properties needs to be understood before the accuracy of the algorithm can be determined. To this end, the objectives of our coccolith studies during this reporting period have been:

- (1) acquire optical field data on the distribution and abundance of coccolithophores in the Gulf of Maine,
- (2) process data from recent cruises, and
- (3) publish earlier results from our remote sensing work done with the CalCOFI data set, flow cytometry experiments, optical experiments with coccoliths, and Gulf of Maine pre-launch cruises.

For perspective on the directions of our work, we provide an overview of our previous activities:

Jan-June 1995: Research focus – chemostat cultures (in which algal growth rate was precisely controlled) and we examined how the optical properties of these calcifying algae changed as a function of growth.

Semi-Annual Report (1 July – 31 December 1997) NAS5-31363

July-Dec 1995: Research focus – shipboard measurements of suspended calcite and estimates of optical backscattering as validation of the laboratory measurements. We participated on two month-long cruises to the Arabian sea, measuring coccolithophore abundance, production, and optical properties.

Jan-June 1996: Research focus – field calcite distributions, during two Gulf of Maine cruises, one in March and one in June.

July-Dec 1996: Research focus – participated on another cruise to the Gulf of Maine and processed samples from the Gulf of Maine.

Jan-June 1997: Research focus – continued processing samples from our previous cruises, upgraded our laser light scattering photometer used in all of the calcite scattering measurements, performed another pre-launch cruise on calcite particle optics in the Gulf of Maine, and analyzed our results from the MODIS-funded flow cytometer work.

b. Work Accomplished:

1) Processing of the suspended calcite samples from the June '97 cruise. We processed the CHN samples from this last trip, which will be important for understanding the backscattering arising from suspended organic matter.

2) Final analysis and write-up of our flow cytometer experiments. In October '97, this manuscript was submitted for the MODIS special issue to appear in J. Geophys. Res. next year.

3) Continued microscope cell/coccolith counts for samples from the Gulf of Maine. We are processing count data from '96, and working on enumeration of '97 samples.

4) A paper on coccolith optics with Ken Voss and Katherine Kilpatrick, has been reviewed, revised, and sent back to Limnology and Oceanography. It should appear in print in 6-9 months. The paper deals with a laboratory comparison of volume scattering instruments, using the coccolithophore, *Emiliana huxleyi*, and how to model the optical properties.

5) We performed a pre-launch MODIS cruise in the Gulf of Maine aboard the R/V Delaware II, and as with our previous Albatross cruise, weather conditions were extremely bad (up to 50kt winds and 20 foot seas). We ran our underway system for the entire trip (~ 1700 nautical miles) without a problem. On this cruise, we provided sea truth radiance and irradiance data for the

Semi-Annual Report (1 July – 31 December 1997) NAS5-31363

SeaWiFS (with imagery coordinated with Dr. Gene Feldman). We visited 60 stations, 28 of which were full optical stations (with measurements of total backscattering, acid-labile backscattering, calcite concentrations, coccolithophore and coccolith counts). We had the Yentsch/Phinney group on board measuring spectral absorption, in situ absorption/attenuation (AC-9), upwelling and downwelling irradiance (SATLANTIC TSRB bio-optical sampler), and dissolved organic matter absorption. We had 5 days with clear conditions, and radiometers in the water for the SeaWiFS overpass.

6) Suspended calcite samples from the Gulf of Maine have been run in the graphite furnace atomic absorption spectrometer at the University of Maine. We now only have samples from our most recent cruise in November '97.

7) All cell and coccolith counts from the Arabian Sea are now being analyzed for publication. The first sections of coccolith concentration are now complete, and show some fascinating trends. Data from JGOFS Process Cruise 6 are now entered into spreadsheets. In terms of current microscopy, we now are focusing on the several hundred cell count samples from our 1997 Gulf of Maine cruises. This will take several months to complete.

8) Calcification data from the March, June and November 1996 Gulf of Maine cruises have been analyzed and the first draft of a manuscript is now complete. The manuscript will be submitted for publication following final changes.

c. Data/Analysis/Interpretation:

Single cell experiments:

The results of our calcite flow cytometry work have been submitted for publication in the MODIS special issue of JGR-Oceans.

Cruise results:

As with our June '97 cruise, calcite-dependent backscattering was quite high in the Gulf of Maine during November, 1997. This cruise was the first late Fall cruise in the Gulf of Maine, where calcium carbonate optical properties were quantified. Calcite scattering commonly accounted for 10-20% of total backscattering. Interestingly, even with the low light conditions, coccolithophores were still remarkably abundant in the Gulf of Maine. We formerly interpreted strong coccolith influence on particle optics as a "summer-only" issue but it now can be clearly considered a year-round phenomenon.

Semi-Annual Report (1 July – 31 December 1997) NAS5-31363

Given the future plan for more Gulf of Maine cruises, as well as our SIMBIOS activities, we are writing new software to merge the various data sets into one file that can be submitted to NASA's Sea Bass data archive. The first version of the software (which performs vicarious calibrations, offset corrections, plus calculating "derived quantities" is now complete. This software will considerably reduce the time currently required to quality control the numbers and produce hydrographic plots of the data.

The March, June and November cruises to the Gulf of Maine were processed to show the aerial distribution and depth profiles of calcification, primary productivity, and calcite concentrations. These results represent the largest assemblage of their kind in the Gulf of Maine, and are featured in the manuscript currently in draft form.

d. Anticipated Future Actions:

Work in the next year will address several areas:

- 1) Processing of the suspended calcite samples from the November '97 cruise.
- 2) Any necessary revision of our flow cytometer manuscript.
- 3) Continued microscope cell/coccolith counts for samples from the Gulf of Maine.
- 4) We will go to sea in June '98 on yet another MODIS Gulf of Maine cruise.

e. Problems/Corrective Actions: None

f. Publications:

Voss, K., W. M. Balch, and K. A. Kilpatrick. Scattering and attenuation properties of *Emiliana huxleyi* cells and their detached coccoliths. *Limnol. Oceanogr.* (In press).

Balch, W. M. and B. Bowler. Sea surface temperature gradients, baroclinicity, and vegetation gradients in the sea. *J. Plank. Res.* (In press).

Balch, William M., David T. Drapeau, Terry L. Cucci, and Robert D. Vaillancourt, Katherine A. Kilpatrick, Jennifer J. Fritz. Optical Backscattering by Calcifying Algae. *J. Geophys. Res.* (Submitted).

Semi-Annual Report (1 July – 31 December 1997) NAS5-31363

Campbell, J., D. Antoine, R. Armstrong, W. Balch, R. Barber, and others. Comparison of algorithms for estimating primary productivity from surface chlorophyll temperature and irradiance. *Global Biogeochem. Cycles* (In preparation).

Graziano, L., W. Balch, D. Drapeau, B. Bowler, and S. Dunford. Organic and inorganic carbon production in the Gulf of Maine. *Cont. Shelf Res.* (In preparation).

Fritz, J. and W. Balch. Verification of carbon-14 calcification rates of the coccolithophore *Emiliana huxleyi* using scanning electron microscopy. (In preparation).

7. Other Activities.

The PI participated in the SIMBIOS meeting in Maryland in August, the MODIS Science Team Meeting in October, and a SeaWiFS data acceptance review in November. K. Voss participated in an INDOEX planning meeting in September, and a SIMBIOS remote-sensing-reflectance workshop in Norfolk in December.

Two papers were presented at the AGU Fall Meeting in San Francisco. They are provided below.

J. Ritter, K. Voss, H. Gordon, D. Clark, and L. Koval, Solar Aureole Measurements of Volcanic Aerosol in the Kilauea Plumb, *EOS Transactions*, 78-46, A41A-27.

E.J. welton and K.J. Voss, Preliminary Lidar Results from the Aerosol Characterization Experiment-2 (ACE-2), *EOS Transactions*, 78-46, A41A-13.

8. 1997 Publications.

H.R. Gordon, T. Zhang, F. He, and K. Ding, Effects of stratospheric aerosols and thin cirrus clouds on atmospheric correction of ocean color imagery: Simulations, *Applied Optics*, **36**, 682–697 (1997).

H.R. Gordon, Atmospheric Correction of Ocean Color Imagery in the Earth Observing System Era, *Jour. Geophys. Res.*, **102D**, 17081–17106 (1997).

H. Yang and H.R. Gordon, Remote sensing of ocean color: Assessment of the water-leaving radiance bidirectional effects on the atmospheric diffuse transmittance, *Applied Optics*, **36**, 7887–7897 (1997).

H.R. Gordon, T. Du, and T. Zhang, Remote sensing ocean color and aerosol properties: resolving the issue of aerosol absorption, *Applied Optics*, **36**, 8670–8684 (1997).

H.R. Gordon, T. Du, and T. Zhang, Atmospheric Correction of Ocean Color Sensors: Analysis of the Effects of Residual Instrument Polarization Sensitivity, *Applied Optics*, **36**, 6938–6948 (1997).

T. Zhang and H.R. Gordon, Columnar aerosol properties over oceans by combining surface and aircraft measurements: sensitivity analysis, *Applied Optics*, **36**, 2650–2662 (1997).

T. Zhang and H.R. Gordon, Retrieval of elements of the columnar aerosol scattering phase matrix from sky radiance over the ocean: simulations, *Applied Optics*, **36**, 7948–7959 (1997).

D.K. Clark, H.R. Gordon, K.J. Voss, Y. Ge, W. Broenkow, and C. Trees, Validation of Atmospheric Correction over the Oceans, *Jour. Geophys. Res.*, **102D** 17209–17217 (1997).

K.J. Voss and Y. Liu, Polarized radiance distribution measurements of skylight: Part 1, system description and characterization, *Applied Optics* **36**, 6083–6094 (1997).

Y. Liu and K.J. Voss, Polarized radiance distribution measurements of skylight: Part 2, experiment and data, *Applied Optics* **36**, 8753–8764 (1997).

K.D. Moore, K.J. Voss, and H.R. Gordon, Spectral reflectance of whitecaps: Instrumentation, calibration, and performance in coastal waters, *Jour. Atmos. Ocean. Tech.* (In Press).

H.R. Gordon, In-orbit calibration strategy of ocean color sensors, *Remote Sensing of Environment* (In Press).

Balch, W. M. and B. Bowler. Sea surface temperature gradients, baroclinicity, and vegetation gradients in the sea. *J. Plank. Res.* (In Press).

Semi-Annual Report (1 July – 31 December 1997) NAS5-31363

H. Yang and H.R. Gordon, Retrieval of the Columnar Aerosol Phase Function and Single Scattering Albedo from Sky Radiance over Land: Simulations, *Applied Optics* (Accepted).

Voss, K., W. M. Balch, and K. A. Kilpatrick. Scattering and attenuation properties of *Emiliana huxleyi* cells and their detached coccoliths. *Limnol. Oceanogr.* (In press).

Balch, W. M. and B. Bowler. Sea surface temperature gradients, baroclinicity, and vegetation gradients in the sea. In press, *J. Plank. Res.* (In press).

Balch, William M., David T. Drapeau, Terry L. Cucci, and Robert D. Vaillancourt, Katherine A. Kilpatrick, Jennifer J. Fritz. Optical Backscattering by Calcifying Algae. *J. Geophys. Res.* (Submitted).

Appendix

**Atmospheric correction of ocean color imagery:
Use of the Junge power-law aerosol size distribution with
variable refractive index to handle aerosol absorption**

Abstract

When strongly-absorbing aerosols are present in the atmosphere, the usual two-step procedure of processing ocean color data — (1) atmospheric correction to provide the water-leaving reflectance (ρ_w), followed by (2) relating ρ_w to the water constituents — fails and simultaneous estimation of the ocean and aerosol optical properties is necessary. We explore the efficacy of using a very simple model of the aerosol — a Junge power-law size distribution consisting of homogeneous spheres with arbitrary refractive index — in a nonlinear optimization procedure for estimating the relevant oceanic and atmospheric parameters for Case 1 waters. Using simulated test data generated from more realistic aerosol size distributions (sums of log-normally distributed components with different compositions), we show that the ocean’s pigment concentration (C) can be retrieved with good accuracy in the presence of weakly- or strongly-absorbing aerosols. However, because of significant differences in the scattering phase functions for the test and power-law distributions, large error is possible in the estimate of the aerosol optical thickness. The positive result for C suggests that the detailed shape of the aerosol scattering phase function is not relevant to the atmospheric correction of ocean color sensors. The relevant parameters are the aerosol single scattering albedo and the spectral variation of the aerosol optical depth. We argue that the assumption of aerosol sphericity should not restrict the validity of the algorithm, and suggest an avenue for including colored aerosols, e.g., wind-blown dust, in the procedure. A significant advantage of the new approach is that realistic multi-component aerosol models are not required for the retrieval of C .

1. Introduction

It is now generally recognized that measurement of the radiance reflected from the ocean atmosphere system can be used to estimate the concentration of phytoplankton pigments, the sum of the concentrations of chlorophyll *a* and phaeophytin *a*, in the ocean.¹⁻³ (At present, this estimation is generally limited to Case 1 waters,³ i.e., waters in which phytoplankton and their immediate detrital material constitute the variable component of the water's optical properties.) Thus several sensors have been, or are soon to be, launched for the purpose of studying the spatial-temporal variation of phytoplankton globally, to understand the role of phytoplankton and their variability in global climate. The sea-viewing wide-field-of-view sensor⁴ (SeaWiFS) was launched on August 1, 1997, and the moderate resolution imaging spectroradiometer⁵ (MODIS) is scheduled for launch in the summer of 1998. In Case 1 waters, the component of the measured radiance that carries information about the phytoplankton concentration, the radiance backscattered *out* of the water and transmitted to the top of the atmosphere (the water-leaving radiance), is at most 10% in the blue and typically much smaller in the green. The rest of the signal is comprised of radiance reflected from the atmosphere and the sea surface. Thus, the water-leaving radiance must be extracted from the measured radiance — a process referred to as atmospheric correction.

Typically, atmospheric correction algorithms assume that radiative transfer in the ocean and atmosphere can be decoupled, i.e., photons are never backscattered out of the ocean more than once.⁶ Furthermore, determination of the phytoplankton pigment concentration is carried out in two steps: (1) the water-leaving radiance is retrieved as a product of the atmospheric correction; and (2) the pigment concentration is determined from the water-leaving radiance. The atmospheric correction algorithm has increased in complexity from the simple single-scattering algorithm^{7,8} used for the coastal zone color

scanner (CZCS) — the proof-of-concept ocean color mission — to the complete multiple-scattering algorithm proposed for SeaWiFS.^{9,10} The new algorithm is capable of providing the water-leaving radiance with the required accuracy for typical marine atmospheres; however, it fails when the atmosphere contains strongly-absorbing aerosols, e.g., in the presence of urban pollution or desert dust transported over the ocean by the winds.

Recently, Gordon, Du, and Zhang¹¹ proposed an algorithm for Case 1 waters that is capable of atmospheric correction in the presence of both weakly- and strongly-absorbing aerosols. In this algorithm, the aerosol properties and the pigment concentration are determined simultaneously. This simultaneous determination is required because the aerosol absorption is manifest mostly in the blue, where the water-leaving radiance is usually largest, and the most variable. In effect, in this algorithm the ocean pigment concentration and the aerosol model are systematically varied and the top-of-the-atmosphere (TOA) radiance is computed. The candidate aerosol models used in this algorithm were derived from the bimodal log-normal aerosol size distributions and refractive indices provided by Shettle and Fenn¹² as a function of relative humidity (RH). The water-leaving radiance was computed as a function of the pigment concentration (C) and a marine particulate scattering factor (b^0) using the semi-analytic model of Gordon et al.¹³ The mean of the ocean-atmosphere properties that yield the ten-best fits (in an RMS sense) of the computed to the measured radiances provides the derived parameters (pigment concentration, aerosol optical thickness, aerosol single scattering albedo, etc.).

Zhao and Nakajima¹⁴ proposed a similar algorithm for CZCS, i.e., the aerosol properties and the pigment concentration determined simultaneously; however, because of the severe limitation of the number of spectral bands on CZCS, they employed models with Junge¹⁵ power-law size distributions with a single index of refraction, and used ratios of water-leaving radiances rather than the water-leaving radiance itself. They showed good retrievals with simulated test data created using bimodal aerosol size distributions with

the same index of refraction as the Junge power-law distribution, and concluded that the power-law distribution was an adequate approximation to the now-favored bimodal aerosol distributions for the purposes of atmospheric correction. In contrast to bimodal log-normal size distributions, which require several parameters to describe (the modal diameters and standard deviations of both modes along with their relative concentrations), the simplicity of the Junge power-law distribution is attractive in that only one parameter is required. A further simplification is that the bimodal distributions require an index of refraction for each mode (typically different), while a single refractive index is usually assumed for the power-law distribution.

In this paper, we explore replacing the Shettle and Fenn¹² candidate aerosol bimodal models in the Gordon, Du, and Zhang¹¹ procedure with a Junge power-law model; however, in order to be able to deal with both weakly- and strongly-absorbing aerosols, we let the real and imaginary parts of the index of refraction vary as well as the size distribution parameter — a natural extension of the Zhao-Nakajima¹⁴ algorithm. Thus, all of the properties of the aerosol are allowed to vary continuously, subject to the constraint of the given mathematical form for the aerosol size distribution. This allows use of nonlinear optimization techniques to effect a solution. The results show that excellent retrievals of the pigment concentration are obtained, weakly- and strongly-absorbing aerosols are easily identified, but the retrieved aerosol optical thickness can have large errors because of the significant differences in the scattering phase functions for bimodal log-normal and power-law distributions. Thus, we also answer the question, is a correct aerosol phase function really required for atmospheric correction of ocean color imagery?

We begin with a description of the aerosol and ocean models used in the procedure and describe the nonlinear optimization. Next, we provide tests with simulated data that is free of radiometric calibration errors, and follow with an examination of the effect of realistic

radiometric calibration errors. Finally, we examine the performance of the algorithm as a function of the aerosol's vertical distribution.

2. The correction mechanics

We begin by using a generalized reflectance ρ in place of radiance L . These are related by $\rho = \pi L / F_0 \cos \theta_0$, where F_0 is the extraterrestrial solar irradiance and θ_0 is the solar zenith angle. Then, after avoiding sun glitter and correcting for the presence of whitecaps, the remaining upwelling reflectance at the top of the atmosphere $\rho_t(\lambda)$ consists of the following components:¹⁰ the pure Rayleigh (molecular) scattering contribution $\rho_r(\lambda)$, the pure aerosol scattering contribution $\rho_a(\lambda)$, the contribution due to the interaction effect between air molecules and aerosols $\rho_{ra}(\lambda)$, and the desired water-leaving contribution $t(\lambda)\rho_w(\lambda)$, i.e.,

$$\rho_t(\lambda) = \rho_r(\lambda) + \rho_a(\lambda) + \rho_{ra}(\lambda) + t(\lambda)\rho_w(\lambda), \quad (1)$$

where $t(\lambda)$ is the diffuse transmittance of the atmosphere. As $\rho_r(\lambda)$ can be computed precisely from an estimate of the surface atmospheric pressure,^{16,17} it can be subtracted from $\rho_t(\lambda)$ to form

$$[\rho_t(\lambda) - \rho_r(\lambda)] = [\rho_a(\lambda) + \rho_{ra}(\lambda)] + [t(\lambda)\rho_w(\lambda)]. \quad (2)$$

Following Gordon, Du, and Zhang,¹¹ we use an atmospheric model to compute $\rho_a(\lambda) + \rho_{ra}(\lambda)$ and $t(\lambda)$, an ocean model to compute $\rho_w(\lambda)$, and compare the results to the given value of $\rho_t(\lambda) - \rho_r(\lambda)$.

A. The water and aerosol models

The water reflectance model is derived from Gordon et al.,¹³ and is identical to that employed by Gordon, Du, and Zhang.¹¹ It has two parameters C , the pigment concentration, and b^0 a parameter related to particulate scattering.³ The model assumes that the upwelling spectral radiance below the sea surface is totally diffuse, contrary to the observations of Morel and co-workers.^{18–21} However, as Morel and Gentili²¹ have shown, bidirectional effects can be easily introduced into the model and described as a function of C (and, if necessary, b^0).

The aerosol model utilizes a Junge power-law size distribution:

$$\begin{aligned}\frac{dN}{dD} &= K, & D_0 < D \leq D_1, \\ &= K \left(\frac{D_1}{D} \right)^{\nu+1}, & D_1 < D \leq D_2, \\ &= 0, & D > D_2,\end{aligned}$$

where dN is the number of particles per unit volume with diameters between D and $D + dD$. In this paper, we choose $D_0 = 0.06 \mu\text{m}$, $D_1 = 0.20 \mu\text{m}$, and $D_2 = 20 \mu\text{m}$. The size distribution is thus characterized by a single parameter, ν . A refractive index $m = m_r - im_i$ is then combined with this size distribution to compute the aerosol optical properties — the phase function, optical thickness ($\tau_a(\lambda)$), and single scattering albedo ($\omega_0(\lambda)$) — using Mie theory. As the synthetic test data is also computed from bimodal aerosol models using Mie theory (Subsection 3A), this procedure does not introduce any error, i.e., we assume all particles are spherical. The aerosol optical properties are then used to generate the reflectance $\rho_a(\lambda) + \rho_{ra}(\lambda)$ as a function of the aerosol optical thickness for all viewing-sun geometries. A two-layer radiative transfer code (aerosols in the lower layer) in which the air-sea interface is modeled by a flat Fresnel-reflecting surface, is used in the computations. These reflectances are stored in the form of lookup tables (LUTs) for rapid access by the algorithm. In our LUTs, the values of the parameter ν range from 2 to 4.5 in steps of 0.5, and $m_i = 0, 0.001, 0.003, 0.01, 0.03$, and 0.04 , with $m_r = 1.333$

and 1.50. Thus, we have a total of 72 distinct power-law aerosol models that can be used to interpolate for arbitrary values of ν , m_r , and m_i . We use linear interpolation for ν and quadratic interpolation for m_r and m_i [Formula 25.2.66 of Ref. 22].

In the optimization procedure, there are a total of six parameters: C and b^0 for the water, ν , m_r , m_i , and $\tau_a(865)$, for the atmosphere. [The aerosol optical thickness at 865 nm, $\tau_a(865)$, is the measure of the aerosol concentration.] However, we can reduce the number of parameters by noting that $\rho_w \approx 0$ in the near infrared (NIR). [SeaWiFS has NIR bands at 765 and 865 nm, while MODIS has bands at 748 and 869 nm.] For these bands, the value of $\rho_a(\lambda) + \rho_{ra}(\lambda)$ is known. The spectral variation of $\rho_a(\lambda) + \rho_{ra}(\lambda)$ in the NIR has been shown to depend mostly on the aerosol size distribution and only slightly on the refractive index,¹⁰ thus, these two bands can be used to determine the size distribution parameter ν . This is effected by comparing the measured value of

$$\varepsilon'(\lambda_s, \lambda_\ell) = \frac{\rho_a(\lambda_s) + \rho_{ra}(\lambda_s)}{\rho_a(\lambda_\ell) + \rho_{ra}(\lambda_\ell)}, \quad (3)$$

where λ_s and λ_ℓ are the shorter and the longer of the two NIR bands available on the sensor, with that computed from the models as a function of ν . Figure 1 shows an example of the relationship between ν and $\varepsilon'(765, 865)$ for the power-law distributions. The figure was prepared using the 12 values of the complex refractive index and four values of $\tau_a(865)$. It shows that a coarse estimate of ν (maximum error $\sim +0.3$ to -0.1 , standard error $\sim +0.15$ to -0.1) can be obtained from the measured $\varepsilon'(765, 865)$. Given the value of ν determined from the ν - $\varepsilon'(765, 865)$ relationship for the given geometry, it is a simple matter to compute the aerosol optical thickness that provides the correct value of reflectance at λ_ℓ for each $m_r - im_i$. Thus, both ν and $\tau_a(865)$ can be removed from the list of unknown parameters via the NIR measurements. In the case of SeaWiFS, this leaves six bands from which the four remaining parameters must be determined. It should be noted that using this method of reducing the number of parameters introduces some error. For example, if the actual

aerosol model is identical to one of the 72 candidate models, a close, but incorrect, value of ν will usually be chosen by the algorithm.

B. The nonlinear optimization.

Before continuing the discussion we introduce some simplifying notation:

$$\begin{aligned}\rho'_A(\lambda_i; m_i, m_r) &\equiv \rho_a(\lambda_i; m_i, m_r) + \rho_{ra}(\lambda_i; m_i, m_r) \\ \rho'_W(\lambda_i; C, b^0) &\equiv t(\lambda_i) \rho_w(\lambda_i; C, b^0),\end{aligned}\tag{4}$$

where ρ'_A is the resulting reflectance of the aerosol and interaction term computed at λ_i for the Junge power-law size distribution with the parameters ν and $\tau_a(865)$ (both determined as in Subsection 2A) using m_i and m_r , and ρ'_W is the diffusely transmitted normalized water-leaving reflectance computed at λ_i for water parameters C and b^0 . The assumption that $\rho'_A(\lambda_i; m_i, m_r)$ and $\rho'_W(\lambda_i; C, b^0)$ form the final reflectance field on the top of the atmosphere (TOA) independently leads to the system of nonlinear equations in four variables (m_i, m_r, C, b^0):

$$\left\{ \begin{array}{l} \rho'_A(\lambda_1; m_i, m_r) + \rho'_W(\lambda_1; C, b^0) = \rho_t(\lambda_1) - \rho_r(\lambda_1) \\ \rho'_A(\lambda_2; m_i, m_r) + \rho'_W(\lambda_2; C, b^0) = \rho_t(\lambda_2) - \rho_r(\lambda_2) \\ \dots\dots\dots \\ \rho'_A(\lambda_{N_v}; m_i, m_r) + \rho'_W(\lambda_{N_v}; C, b^0) = \rho_t(\lambda_{N_v}) - \rho_r(\lambda_{N_v}). \end{array} \right.\tag{5}$$

We seek to solve this set of equations for m_i , m_r , C , and b^0 when N_v , the number of visible bands used in the retrieval, is greater than the number of unknowns (4), and adopt a nonlinear optimization procedure in order to do so. We note that the set of variables (m_i, m_r, C, b^0) is subject to the constraints:

$$\left\{ \begin{array}{l} 0 \leq m_i(\min) \leq m_i \leq m_i(\max) \\ 0 < m_r(\min) \leq m_r \leq m_r(\max) \\ 0 < C(\min) \leq C \leq C(\max) \\ 0 < b^0(\min) \leq b^0 \leq b^0(\max). \end{array} \right.\tag{6}$$

As in Gordon, Du, and Zhang,¹¹ we assume that $C(min) = 0.05 \text{ mg/m}^3$, $C(max) = 1.50 \text{ mg/m}^3$, $b^0(min) = 0.12 \text{ m}^{-1}$, and $b^0(max) = 0.45 \text{ m}^{-1}$. For the atmosphere, we take $m_i(min) = 0$, $m_i(max) = 0.04$, $m_r(min) = 1.33$, and $m_r(max) = 1.50$, as realistic ranges for the aerosol parameters. We choose as the the least-square objective function:

$$S_{LSQ}^2(m_i, m_r, C, b^0) = \frac{1}{(N_v - 1)} \sum_{i=1}^{N_v} \left(\frac{\rho'_A(\lambda_i; m_i, m_r) + \rho'_W(\lambda_i; C, b^0)}{\rho_t(\lambda_i) - \rho_r(\lambda_i)} - 1 \right)^2. \quad (7)$$

At the solution point $(m_i^*, m_r^*, C^*, b^{0*})$, S_{LSQ} should attain its minimal value subject to constraints Eq. (6).

A number of versatile methods exists to find such a solution²³ although they might differ appreciably as to the convergence rate, the memory requirements, and the ability to converge to the solution. In particular, methods belonging to the so-called *quasi-Newton* class,²⁴ that take advantage of the information contained in the Hessian matrix of a function (i.e., the square matrix of the second partial derivatives of the function evaluated at a point) in calculating the step size and the direction of search, appear to be adequate for our purposes. Powell²⁵ proves the convergence to a minimum for the Davidon-Fletcher-Powell (DFP) *variable metric* class method [which also holds for Broyden-Fletcher-Goldfarb-Shanno (BFGS) algorithm] on a function with properties outlined above [Eqs. (5) and (6)]. However, to the best of our knowledge, the quasi-Newton class methods do not guarantee, in general, a convergence to a minimum. In this study we used DZXMWD routine from the commonly available IMSL library,²⁶ which is based on the Harwell library routine VA10A and incorporates a quasi-Newton method. To assure the convergence to a minimum in our non-linear optimization procedure a set of starting search points is taken, some of which are discarded after performing a few iterations based on their relative values. We observed that the resulting solution was the same (within a pre-set tolerance) whatever the number of starting search points were chosen, meaning that convergence to a *global*

minimum was probably achieved, so we believe it is sufficient to use just one starting point in solving the system [Eq. (5)] and the result is the solution we want.

3. Algorithm performance with simulated data.

A. Characteristics of the simulated $\rho_i(\lambda)$ data.

As in earlier work,^{9,11} we tested the performance of the algorithm with simulated data — pseudodata. The pseudodata were created by choosing specific values of C and b^0 for the computation of $\rho_w(\lambda)$, and by utilizing specific aerosol models for the computation of $\rho_r + \rho_a + \rho_{ra}$. The aerosol models we chose for the tests were those developed by Shettle and Fenn¹² at a relative humidity of 80%. For these the size frequency distribution is written

$$\frac{dN}{dD} = \sum_{i=1}^M \frac{dN_i}{dD} \quad (8)$$

where, dN_i is the number of particles per unit volume per with diameter between D and $D + dD$ of the i^{th} species or component. The individual components are taken to be log-normally distributed,¹²

$$\frac{dN_i}{dD} = \frac{N_i}{\log_e(10)\sqrt{2\pi}\sigma_i D} \exp \left[-\frac{1}{2} \left(\frac{\log_{10}(D/D_i)}{\sigma_i} \right)^2 \right], \quad (9)$$

where, D_i , and σ_i are the modal diameter and the standard deviation, respectively, and N_i is the total number density of the i^{th} component. Table 1 provides the parameters N_i , D_i , σ_i , and $m_r - im_i$ for each test aerosol model. The nomenclature M80, C80, T80, and U80, refers to the Maritime, Coastal, Tropospheric, and Urban aerosol models¹² at 80% relative humidity. Figure 2 provides the spectral variation in τ_a for the four test aerosol models. Note that the spectral variation of the test data is enclosed within the range of the candidate aerosol set, for which $\tau_a(\lambda)/\tau_a(865) \approx (865/\lambda)^{(\nu-2)}$. To provide a sense of how well the candidate size distribution approximates the test distributions, Figure 3

compares the volume size distribution $dV/d\ln D$ of three of the four test models (solid curves) with that for the Junge power-law distribution (dotted curves). In Figure 3, all volume distributions are normalized such that $\int_0^\infty dN = 1$. Because of their bimodality, M80 and U80 can be better represented by Junge power-law distributions than T80. Table 2 provides the single-scattering albedo for the test models. Clearly, U80 absorbs much more strongly than the others, which we refer to as “weakly” absorbing.

A test data set was simulated by computing $\rho_t(\lambda) - t(\lambda)\rho_w(\lambda)$ for the M80, C80, T80, and U80 aerosol models with $\tau_a(865) = 0.1, 0.2, \text{ and } 0.3$, and $\rho_w(\lambda)$ with $b^0 = 0.3 \text{ m}^{-1}$ (the adopted mean value³ for Case 1 waters) and $C = 0.1, 0.5, \text{ and } 1.0 \text{ mg/m}^3$. Note that for the test data, the aerosol optical thickness at 412 nm can be as high as 0.80 for T80 (Figure 2). The simulated data were created for solar zenith angles (θ_0) of $0^\circ, 20^\circ, 40^\circ, \text{ and } 60^\circ$, with the sensor viewing at an angles (θ) of $\approx 1^\circ$ and $\approx 45^\circ$ with respect to nadir and an azimuth (ϕ) of 90° relative to the sun. These cover much of the sun-viewing geometry available to an ocean color sensor. The combination $\theta_0 = 0$ and $\theta \approx 1^\circ$ is excluded, as it would be within the sun’s glitter pattern, so there are a total of seven sun-viewing geometries considered.

B. Retrieval results for error-free ρ_t .

In this subsection, we examine the performance of the algorithm when the TOA reflectance ρ_t is free of error. Examples of the retrieval of the spectra of $\rho_a + \rho_{ra}$ and $t\rho_w$, along with the true values and the recovered values of the parameters, are provided in Figure 4 for two different sun-viewing geometries and pseudodata generated using two different aerosol models (M80 and U80). The retrievals were effected using the first five SeaWiFS bands (412, 443, 490, 510, and 555 nm) in the nonlinear optimization, and 765 and 865 nm to determine ν and $\tau_a(865)$. The results indicate excellent fits between the

measured and reconstructed values of $\rho_t(\lambda) - \rho_r(\lambda)$ are obtained for both the strongly (U80) and weakly (M80) absorbing aerosols. The retrieved $t\rho_w(\lambda)$ is also excellent, with an error at 443 nm less than 0.001 (recall that Gordon and Wang⁹ used as a criterion for the performance of their SeaWiFS algorithm that the error in $t\rho_t$ at 443 nm should be smaller than ± 0.002). Retrievals of C , ω_0 , and b^0 are also excellent. In contrast, the retrieval of $\tau_a(865)$ is sometimes very poor, e.g., Figure 4c and 4d. This failure to derive acceptable values of $\tau_a(865)$ is completely explained by the fact that the scattering phase functions resulting from the Junge power-law distribution do not correspond well to those used in the generation of the pseudodata. Figures 5a and 5b compare the phase functions [$P(\Theta)$, where Θ is the scattering angle] derived in the retrievals, i.e., computed using the retrieved values of ν , m_i , and m_r , with those used in the generation of the pseudodata for Figures 4c and 4d respectively. There are significant differences between the retrieved and true phase functions, and for the geometry in this situation (single scattering angle $\Theta = 120^\circ$) the difference causes the low values of $\tau_a(865)$ obtained by the algorithm.

Figure 6 provides similar results for pseudodata created using the T80 aerosol model. In this case the results are still acceptable, but not as good as those in Figure 4. The degradation in this case is caused partially by the fact that the Junge power-law distribution cannot fit the T80 distribution well (Figure 3), and partially by the fact that the optical thickness in the visible can become very large (Figure 2) causing the reflectances to become very large (compare Figure 6b with Figures 4c and 4d). In spite of the deficiencies of the algorithm, it is remarkable that in Figures 4 and 6, the maximum error in the retrieved value of C is only slightly over 10%.

The performance of the algorithm for other geometries, pigment concentrations, and aerosol optical thicknesses is summarized in Tables 3–5. In these tables, the quantity being retrieved (ω_0 , C , and b^0 for Tables 3, 4, and 5, respectively) is averaged over the seven sun viewing directions, and its standard deviation (S_d) over the seven directions is also

presented along with the error in the averaged quantity (D). A small value for S_d indicates stability in the performance as the sun-viewing geometry is varied. Clearly, it is desirable for both S_d and D to be as small as possible.

The results for ω_0 at 865 nm (Table 3) show that weakly- and strongly-absorbing aerosols are well distinguished; however, the actual derived value of ω_0 is not as accurate as that obtained for the same test data using the Gordon, Du, Zhang¹¹ algorithm (Table 2 in Ref. 11). In particular, larger errors are apparent for the weakly-absorbing aerosols; however, the retrieval is generally improved as $\tau_a(865)$ increases, i.e., as the atmospheric contribution to ρ_t increases.

The retrievals of C (Table 4) are generally excellent, with the largest error being 17.6%. However, the T80 results are poorer than the others — the largest error in the absence of T80 being 10.4%. The error in C increases with increasing $\tau_a(865)$, but not dramatically. Other than a few T80 cases, S_d is generally $< 5\%$ indicating good stability with respect to sun-viewing geometry. Table 5 shows that the retrieval of b^0 can usually be carried out with an error less than 20% (except for T80) with good sun-viewing geometry stability.

We have not tabulated the performance regarding the retrievals of $\tau_a(865)$, as they are significantly poorer than those in Gordon, Du, and Zhang¹¹ due to the strong differences in the Shettle and Fenn¹² and the Junge power-law phase functions (Figure 5).

The quality of the resulting fits of the optimized and TOA pseudorefectances is measured by the value of S_{LSQ} . Table 6 provides the mean value of S_{LSQ} and its standard deviation σ_S over all values of $\tau_a(865)$ and C provided in Tables 3–5, as well as over all sun-viewing geometries (a total of 63 individual determinations for each model used to generate the pseudodata). [The models UU80, U280, and U480 are described later.] The

table shows that excellent fits are obtained with relatively low dispersion. As expected, the error is somewhat larger for the T80 case.

The results of this subsection suggest that the water parameters C and b^0 can be retrieved with reasonably good accuracy. The poorer results for ω_0 and, in particular, for $\tau_a(865)$ are simply manifestations of the fact that, as argued by Wang and Gordon,²⁷ an aerosol model that yields a phase function that correctly approximates the true phase function is required to retrieve accurate values, even for weakly-absorbing aerosols. However, this is apparently not the case if the goal is only to retrieve the water parameters, i.e., a correct representation of the aerosol phase function is not necessary for retrieving water parameters.

C. Retrieval results with calibration error in ρ_t .

To illustrate the influence of radiometric calibration error on the performance of this algorithm, we follow Gordon, Du, and Zhang¹¹ and add error to ρ_t equal to the uncertainty expected after effecting an in-orbit calibration adjustment of the visible bands with respect to the band at λ_t . Gordon²⁸ has shown that for such a procedure, the residual calibration error in all of the bands will have the same sign as that at λ_t , and the magnitude of the error will progressively decrease into the visible, roughly as ρ_r increases. Table 7 provides the estimated residual uncertainty (in %) given an uncertainty of 5% in the radiometry at λ_t . We have added (subtracted) the error in Table 7 to (from) the pseudodata used in Subsection 3B to produce erroneous reflectances. The algorithm was then operated using these reflectances as input pseudodata. Figure 7 provides examples of the retrievals in the presence of these errors. It shows that the retrieval of $\rho_a + \rho_{ra}$ is too large (small) if the radiometric error is positive (negative). Typically, this is compensated by the opposite behavior in $t\rho_w$. To achieve this the algorithm apparently varies b^0 holding C to the

nearly-correct value (compare Figures 7a and 7b with Figure 4c, and Figures 7c and 7d with Figure 4d). Note that the calibration error will cause an incorrect ν to be chosen: a positive (negative) error results in a smaller (larger) ν . The quality of the fits is only marginally degraded from the error-free case. Averaging $\overline{S_{LSQ}}$ for the M80, C80, T80, and U80 in Table 6 yields 0.26%. This is increased only to 0.37% for a negative calibration error (the worse case of the two).

Tables 8 and 9 summarize all of the retrievals in the presence of radiometric calibration error. They should be compared to Table 4. Although there are some systematic variations in C with calibration error, e.g., for $C = 0.1 \text{ mg/m}^3$ the retrieved C tends to be larger (smaller) for a positive (negative) calibration error, it is not systematic over the range of C values or aerosol models. We can conclude from this analysis that the algorithm is relatively insensitive to radiometric calibration error of the magnitude expected after in-orbit calibration adjustment. It is certainly no more sensitive than the Gordon, Du, and Zhang¹¹ algorithm.

D. Influence of aerosol vertical structure on retrieval of C

In the results described in Subsections 3B and 3C, it has been assumed that the aerosol is located in a thin layer near the sea surface, as it has been shown that the vertical structure of the aerosol concentration is irrelevant as long as the aerosol is weakly absorbing.¹⁰ However, when the aerosol is strongly absorbing, this is not the case.^{10,11} In the earlier subsections, the vertical structure of the test pseudodata and the candidate Junge power-law models were identical. In this subsection, we examine the quality of the retrievals when the Urban aerosol is uniformly mixed with air (molecular scattering) from the surface to 2 km (U280), from the surface to 4 km (U480), and uniformly mixed with air from the surface to the TOA (UU80). In contrast, the radiative transfer computations for

the candidate aerosol models still employ a two-layer atmosphere with all aerosol scattering in the lower layer and all molecular scattering in the upper layer.

Figure 8 provides examples of the performance of the algorithm for the U280 and U480 cases with $\theta_0 = 20^\circ$ and $\theta = 1.02^\circ$. These should be compared with Figure 4b for which the pseudodata and the candidate models had the same vertical distribution of aerosol. Note the decreasing quality of the retrievals as the aerosol layer thickens. This is also manifest in a decreasing quality of the fit of the computed reflectances to the pseudodata, i.e., increasing S_{LSQ} , with increased layer thickness (Table 6). Table 10 provides a summary comparing the retrieved C , averaged over sun-viewing geometry, for the U280 and U480 with that for U80. The UU80 retrievals are not shown because the *maximum* value of C allowed (1.5 mg/m^3) was *always* chosen. Note that as the layer thickens, the retrieved values for C increase. This is explained as follows. Increasing the layer thickness causes $\rho_a(\lambda) + \rho_{ra}(\lambda)$ to become increasingly smaller as λ decreases (see Figure 4 of Ref. 11). The algorithm tries to cope with this decrease in absorption by (1) choosing the largest value of m_i available, and (2) increasing C to further reduce $\rho_t(\lambda) - \rho_r(\lambda)$ in the blue relative to the red. The fact that the U280 retrievals were realistic is encouraging. It suggests that the algorithm as presented could handle aerosol vertical structure with only minor changes. The reasoning is as follows. First, as most strongly absorbing aerosols, e.g., wind-blown dust, smoke from biomass burning, etc., are likely to be mixed to altitudes of 2-4 km, it is clear that the simple vertical structure of the atmosphere used in generating the candidate model LUTs (a two-layer model: all aerosol scattering in the lower layer and all molecular scattering in the upper layer) must be modified. Second, since the vertical structure in the case of nonabsorbing or weakly-absorbing aerosols is irrelevant, using LUTs with aerosol mixed higher in the atmosphere will not have a negative impact on the retrieval of C for such aerosols (M80, C80, and T80). Third, the U280 retrievals were good even though the vertical distribution of the aerosol mixing was in error by 2 km. These observations

suggest that if the candidate LUTs were all generated for an aerosol mixed to 2 km, the performance in the case of the M80, C80, T80, and U80, examples would be only slightly degraded, from that in Table 4, while the performance for U480 would be significantly improved over that in Table 10 and that for U280 would be slightly improved. This is the strategy that will be used in implementing the algorithm.

4. Discussion.

The results in this paper are in agreement with the conclusion of Zhao and Nakajima:¹⁴ the Junge power-law aerosol size distribution can be usefully applied to the problem of atmospheric correction of ocean color sensors. However, we have extended their algorithm, in which only a single value of refractive index ($1.50 - i0.01$) was used for both the Junge power-law distribution and the test pseudodata, to allow both m_r and m_i to be determined in the nonlinear optimization procedure. Simulations show that our algorithm yields excellent retrievals of C in atmospheres with either weakly- or strongly-absorbing aerosols, but retrieval of the aerosol optical thickness can show large error. The error in $\tau_a(865)$ is traced to significant differences between the phase functions of the optimized Junge power-law and the test pseudodata (Figure 5). In contrast, Zhao and Nakajima typically obtained excellent $\tau_a(550)$ retrievals (error $\sim 10\%$). This discrepancy is probably due to the fact that they used the same refractive index for all of their computations. Hansen and Travis¹⁶ show that for a fixed refractive index, the phase functions computed for significantly different size distributions can be very similar as long as the size distributions have the same effective radius and effective variance. In our more realistic simulations, in which even the individual components of the log-normal size distributions for the test data [Eqs. (8) and (9)] have different refractive indices [which also depend on λ], this similarity is precluded, preventing an accurate estimate of $\tau_a(865)$.

Our results suggest that the detailed shape of the aerosol scattering phase function is not relevant to atmospheric correction in Case 1 waters, i.e., we can retrieve excellent values of C (Figure 4) with very poor phase functions (Figure 5). Apparently, the most important parameters are ω_0 and the spectral variation of optical thickness, $\tau_a(\lambda)/\tau_a(865)$. [Note that the absolute value of $\tau_a(865)$ is directly dependent on the phase function which is not relevant.] Gordon¹⁰ has already pointed out that the choice of candidate aerosol models in the Gordon and Wang⁹ correction algorithm forces a particular ω_0 - $\tau_a(\lambda)/\tau_a(865)$ relationship to be applied in the correction. In the present algorithm, no such relationship is impressed on the retrievals — ω_0 is determined mostly by ν and m_i , and $\tau_a(\lambda)/\tau_a(865)$ is principally determined by ν .

The fact that excellent retrievals of C are obtained even though the phase function of the resulting aerosol model is a poor approximation to the true phase function (Figure 5) suggests that this algorithm is not limited by the fact that the aerosol optical properties [ω_0 , $\tau_a(\lambda)/\tau_a(865)$, and $P(\Theta)$] are computed assuming the aerosol consists of homogeneous spheres (Mie theory). Mishchenko and co-workers^{29,30} have shown that in the case of randomly oriented spheroids, used as a model for dust-like tropospheric aerosols, the only aerosol optical property that is strongly influenced by the particle shape is the phase function. Thus, for the purpose of retrieving C , the use of Mie theory should not restrict the applicability of the algorithm. In contrast, the retrieved $\tau_a(865)$ depends directly on $P(\Theta)$ and therefore will only be correct if $P(\Theta)$ is correct.²⁷

We have made the implicit assumption that m_i and m_r are constant for the Junge power-law models. This results in only a small variation in ω_0 with λ (Table 2). Unfortunately, some aerosol species, such as wind-blown dust, are colored and show significant variation in m_i (and therefore ω_0) with wavelength.³¹ The algorithm as described above cannot handle these aerosols; however, with minor changes it should be able to. Essentially, all that is needed is to force a prescribed spectral variation in m_r and m_i — which,

along with ν and $\tau_a(865)$ determined as in Subsection 3A, fixes all of the aerosol properties — and vary only C and b_0 until a minimum in S_{LSQ} is reached. If the correct spectral variation in m_r and m_i is chosen, the minimal S_{LSQ} in this case should be considerably smaller than that obtained using wavelength-independent values of m_r and m_i . Thus, a larger-than-expected minimal S_{LSQ} could be employed as a signal that colored aerosols may be present, and that a set of variable- m values should be tested to see if S_{LSQ} can be reduced.

Our proposed method for dealing with the vertical distribution of strongly-absorbing aerosols — placing them in a uniformly mixed layer with a thickness of 2 km in the computations used to generate the Junge power-law LUTs — may not be optimum. Unfortunately, other approaches, such as trying to retrieve the layer thickness using LUTs generated for several layer thicknesses,¹¹ may require too much computer memory to be useful. There were 72 separate aerosol models already used as the basis for our interpolation of $\rho_a + \rho_{ra}$ for arbitrary ν , m_r , and m_i . These require about 500 Mb of random access memory to operate the algorithm. In any event, in the final analysis, all atmospheric correction procedures must compromise in some manner to deal with the problem of absorbing-aerosol vertical structure.

We believe that the principal advantage of the present algorithm over and above that proposed by Gordon, Du, and Zhang¹¹ is the fact that realistic multi-component aerosol models are *not* required for the extraction of ocean properties (although the spectral variation of m will be required for colored aerosols). Unfortunately, by abandoning realistic models in favor of the simpler Junge power-law, we lose some ability to retrieve meaningful aerosol properties, e.g., $\tau_a(865)$.

We are presently studying ways of making this algorithm more efficient, with the goal that it can be applied to the processing of SeaWiFS and MODIS imagery.

Acknowledgement

The authors are grateful for support from the National Aeronautics and Space Administration, Goddard Space Flight Center, under Contracts NAS5-31363 and NAS5-31734.

References

1. H. R. Gordon, D. K. Clark, J. L. Mueller and W. A. Hovis, "Phytoplankton pigments derived from the Nimbus-7 CZCS: initial comparisons with surface measurements," *Science* **210**, 63-66 (1980).
2. W. A. Hovis, D. K. Clark, F. Anderson, R. W. Austin, W. H. Wilson, E. T. Baker, D. Ball, H. R. Gordon, J. L. Mueller, S. Y. E. Sayed, B. Strum, R. C. Wrigley and C. S. Yentsch, "Nimbus 7 coastal zone color scanner: system description and initial imagery," *Science* **210**, 60-63 (1980).
3. H. R. Gordon and A. Y. Morel, *Remote Assessment of Ocean Color for Interpretation of Satellite Visible Imagery: A Review* (Springer-Verlag, New York, 1983), 114 pp.
4. S. B. Hooker, W. E. Esaias, G. C. Feldman, W. W. Gregg and C. R. McClain, *SeaWiFS Technical Report Series: Volume 1, An Overview of SeaWiFS and Ocean Color* (NASA, Greenbelt, MD, Technical Memorandum 104566, July 1992).
5. V. V. Salomonson, W. L. Barnes, P. W. Maymon, H. E. Montgomery and H. Ostrow, "MODIS: Advanced Facility Instrument for Studies of the Earth as a System," *IEEE Geosci. Rem. Sens.* **27**, 145-152 (1989).
6. H. R. Gordon, "Radiative Transfer: A Technique for Simulating the Ocean in Satellite Remote Sensing Calculations," *Applied Optics* **15**, 1974-1979 (1976).

7. H. R. Gordon, "Removal of Atmospheric Effects from Satellite Imagery of the Oceans," *Applied Optics* **17**, 1631–1636 (1978).
8. H. R. Gordon, D. K. Clark, J. W. Brown, O. B. Brown, R. H. Evans and W. W. Broenkow, "Phytoplankton pigment concentrations in the Middle Atlantic Bight: comparison between ship determinations and Coastal Zone Color Scanner estimates," *Applied Optics* **22**, 20–36 (1983).
9. H. R. Gordon and M. Wang, "Retrieval of water-leaving radiance and aerosol optical thickness over the oceans with SeaWiFS: A preliminary algorithm," *Applied Optics* **33**, 443–452 (1994).
10. H. R. Gordon, "Atmospheric Correction of Ocean Color Imagery in the Earth Observing System Era," *Jour. Geophys. Res.* **102D**, 17081–17106 (1997).
11. H. R. Gordon, T. Du and T. Zhang, "Remote sensing of ocean color and aerosol properties: resolving the issue of aerosol absorption," *Applied Optics* **36**, 8670–8684 (1997).
12. E. P. Shettle and R. W. Fenn, *Models for the Aerosols of the Lower Atmosphere and the Effects of Humidity Variations on Their Optical Properties* (Air Force Geophysics Laboratory, Hanscomb AFB, MA 01731, AFGL-TR-79-0214, 1979).
13. H. R. Gordon, O. B. Brown, R. H. Evans, J. W. Brown, R. C. Smith, K. S. Baker and D. K. Clark, "A Semi-Analytic Radiance Model of Ocean Color," *Jour. Geophys. Res.* **93D**, 10909–10924 (1988).

14. F. Zhao and T. Nakajima, "Simultaneous determination of water-leaving reflectance and aerosol optical thickness from Coastal Zone Color Scanner measurements," *Applied Optics* **36**, 6949–6956 (1997).
15. C. Junge, "Atmospheric Chemistry," *Advances in Geophysics* **4**, 1–108 (1958).
16. J. E. Hansen and L. D. Travis, "Light Scattering in Planetary Atmospheres," *Space Science Reviews* **16**, 527–610 (1974).
17. H. R. Gordon, J. W. Brown and R. H. Evans, "Exact Rayleigh Scattering Calculations for use with the Nimbus-7 Coastal Zone Color Scanner," *Applied Optics* **27**, 862–871 (1988).
18. A. Morel and B. Gentili, "Diffuse reflectance of oceanic waters: its dependence on Sun angle as influenced by the molecular scattering contribution," *Applied Optics* **30**, 4427–4438 (1991).
19. A. Morel and B. Gentili, "Diffuse reflectance of oceanic waters. II. Bidirectional aspects," *Applied Optics* **32**, 6864–6879 (1993).
20. A. Morel, K. J. Voss and B. Gentili, "Bidirectional reflectance of oceanic waters: A comparison of modeled and measured upward radiance fields," *Jour. Geophys. Res.* **100C**, 13,143–13,150 (1995).
21. A. Morel and B. Gentili, "Diffuse reflectance of oceanic waters. III. Implication of bidirectionality for the remote sensing problem," *Applied Optics* **35**, 4850–4862 (1996).

22. M. Abramowitz and I. A. Stegun, *Handbook of Mathematical Functions* (Dover Publications, New York, 1970), 1046 pp.
23. R. Fletcher, *Practical Methods of Optimization* Vol.1,2 (John Wiley and Sons, Ltd., 1980).
24. P. E. Gill and W. Murray, "Quasi-Newton Methods for unconstrained optimization," *J. Inst. Maths. Appl.* **9**, 91–108 (1972).
25. M. J. D. Powell, *Some global convergence properties of a variable metric algorithm for minimization without exact line searches*, AERE Harwell Report CSS15, 1975).
26. IMSL, *Reference Manual* Vol.4 (IMSL Inc., 1982).
27. M. Wang and H. R. Gordon, "Estimating aerosol optical properties over the oceans with the multiangle imaging spectroradiometer: Some preliminary studies," *Applied Optics* **33**, 4042–4057 (1994).
28. H. R. Gordon, "In-orbit calibration strategy for ocean color sensors," *Remote Sensing of Environment* **63**, 0000–0000 (1998).
29. M. I. Mishchenko and L. D. Travis, "Light scattering by polydispersions of randomly oriented spheroids with sizes comparable to wavelengths of observation," *Applied Optics* **33**, 7206–7225 (1994).

30. M. I. Mishchenko, L. D. Travis, R. A. Kahn and R. A. West, "Modeling phase functions for dustlike tropospheric aerosols using a shape mixture of randomly oriented spheroids," Jour. Geophys. Res **102D**, 16831–16847 (1997).
31. G. A. d'Almeida, P. Koepke and E. P. Shettle, *Atmospheric Aerosols — Global Climatology and Radiative Characteristics* (A. Deepak Publishing, Hampton, VA, 1991).

Figure Captions

Figure 1. Relationship between $\varepsilon'(765, 865)$ and ν (solid curve) averaged over all combinations of four values of $\tau_a(865)$ (0.1, 0.2, 0.3, and 0.4), six values of m_i (0, 0.001, 0.003, 0.01, 0.03, and 0.04), and two values of m_r (1.333, and 1.50), with $\theta_0 = 20^\circ$ and $\theta = 45.9^\circ$. Dashed curves represent the upper and lower envelopes of the relationship and the dark speckled area represents the standard deviation of the various cases about the mean for the given value of ν .

Figure 2. Spectral variation of the aerosol optical thickness for the models used to generate the test pseudodata.

Figure 3. Comparison between the volume size distribution of the aerosol models used to generate the test pseudodata (solid curves) and the Junge power-law distribution (dotted curves).

Figure 4. Comparison between the given (curves) and the retrieved (symbols) reflectances using the Junge power-law size distribution for $\theta = 1.02^\circ$ (i.e., near nadir): (a) M80 with $\theta_0 = 20^\circ$, (b) U80 with $\theta_0 = 20^\circ$, (c) M80 with $\theta_0 = 60^\circ$, (d) U80 with $\theta_0 = 60^\circ$. Unprimed parameters are the true values, primed parameters are the retrieved values.

Figure 5. Comparison of the true (solid curve) and retrieved (dashed curve) phase functions at 865 nm. The retrieved phase function is used to derive the aerosol optical thickness in Figures 4c and 4d: (a) M80, (b) U80.

Figure 6. Comparison between the given (curves) and the retrieved (symbols) reflectances using the Junge power-law size distribution for $\theta = 1.02^\circ$ (i.e., near nadir): (a) T80 with

$\theta_0 = 20^\circ$, (b) T80 with $\theta_0 = 60^\circ$. Unprimed parameters are the true values, primed parameters are the retrieved values.

Figure 7. Comparison between the given (curves) and the retrieved (symbols) reflectances using the Junge power-law size distribution for $\theta = 1.02^\circ$ (i.e., near nadir) in the presence of the calibration errors in Table 6: (a) M80 with $\theta_0 = 60^\circ$ and positive calibration error, (b) M80 with $\theta_0 = 60^\circ$, and negative calibration error, (c) U80 with $\theta_0 = 60^\circ$ and positive calibration error, (d) U80 with $\theta_0 = 60^\circ$, and negative calibration error. Unprimed parameters are the true values, primed parameters are the retrieved values, and ρ_c represents the calibration error.

Figure 8. Comparison between the given (curves) and the retrieved (symbols) reflectances using the Junge power-law size distribution for $\theta_0 = 20^\circ$ and $\theta = 1.02^\circ$ (i.e., near nadir) for cases in which the aerosol is uniformly mixed with air from the surface to an altitude h : (a) U80 aerosol with $h = 2$ km (U280), (b) U80 aerosol with $h = 4$ km (U480). Unprimed parameters are the true values, primed parameters are the retrieved values.

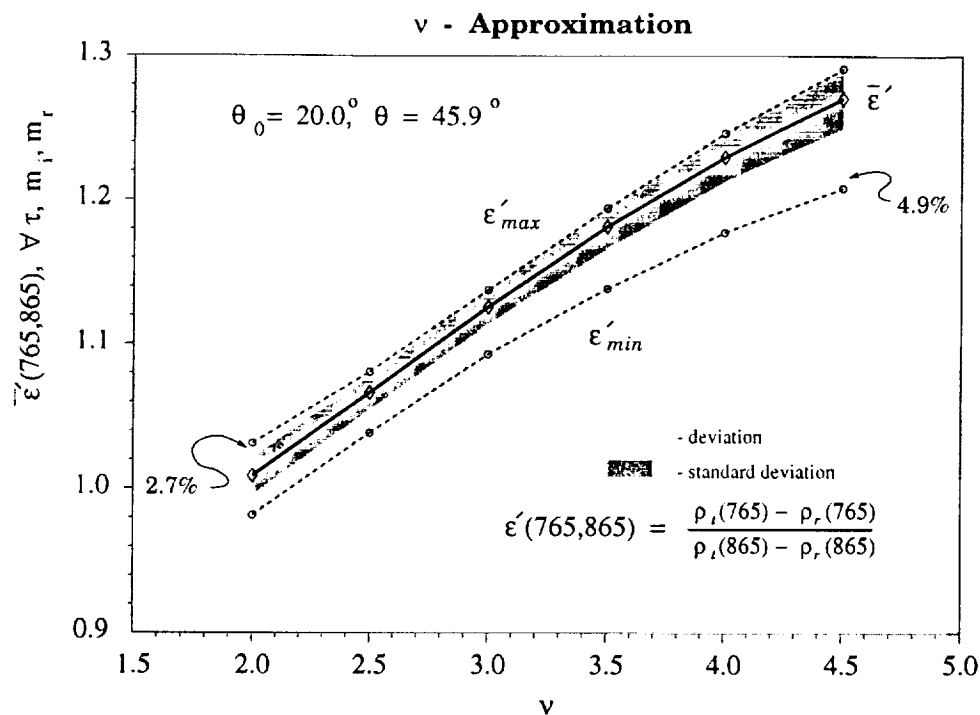


Figure 1. Relationship between $\epsilon'(765,865)$ and ν (solid curve) averaged over all combinations of four values of $\tau_a(865)$ (0.1, 0.2, 0.3, and 0.4), six values of m_i (0, 0.001, 0.003, 0.01, 0.03, and 0.04), and two values of m_r (1.333, and 1.50), with $\theta_0 = 20^\circ$ and $\theta = 45.9^\circ$. Dashed curves represent the upper and lower envelopes of the relationship and the dark speckled area represents the standard deviation of the various cases about the mean for the given value of ν .

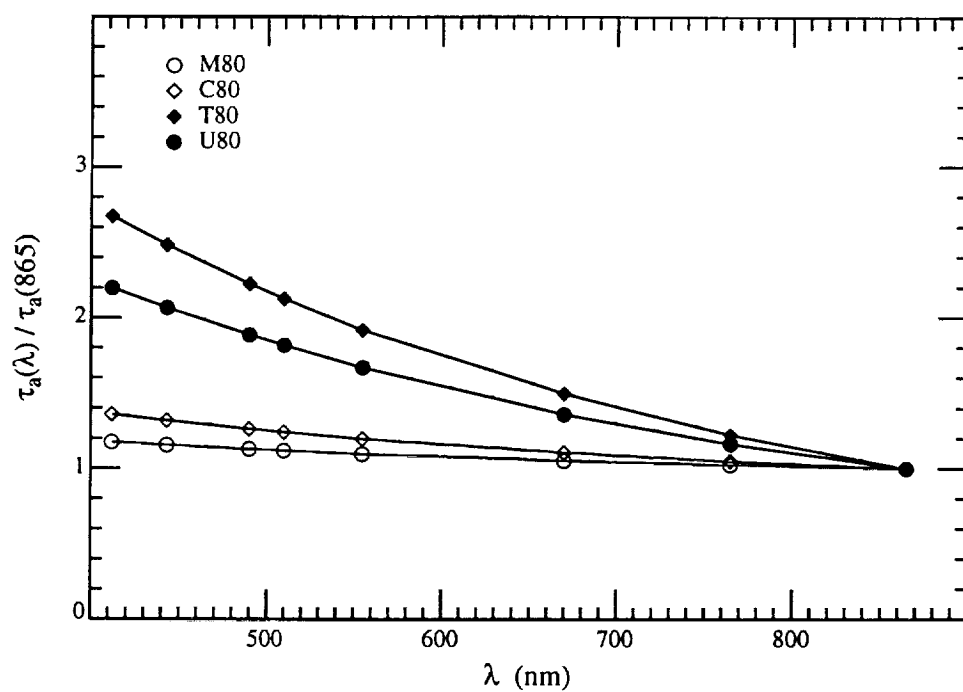


Figure 2. Spectral variation of the aerosol optical thickness for the models used to generate the test pseudodata.

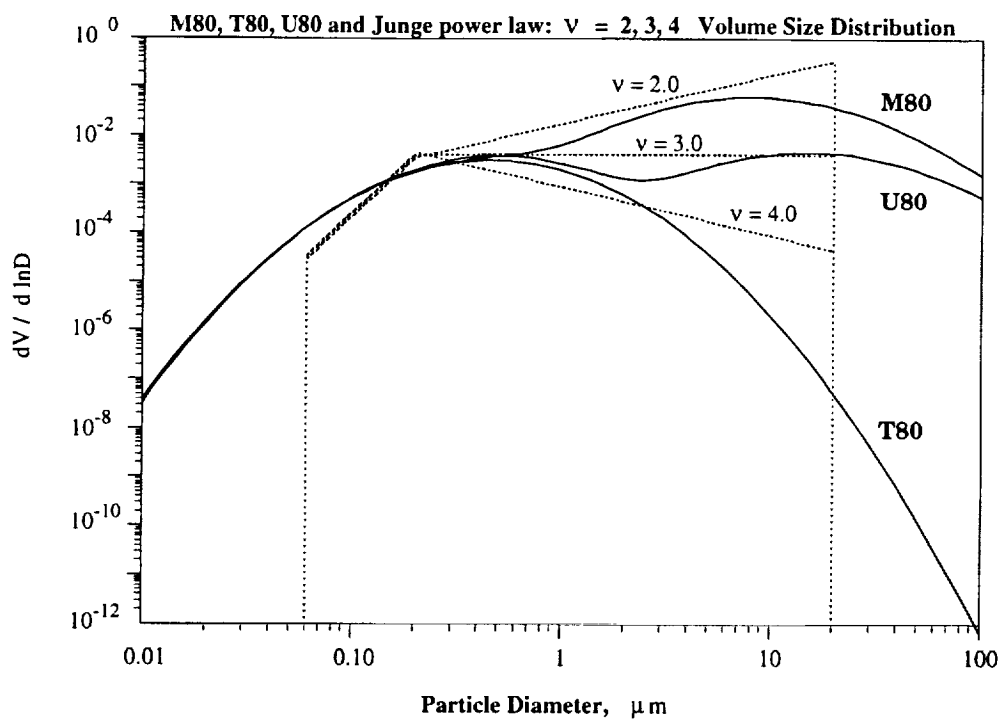
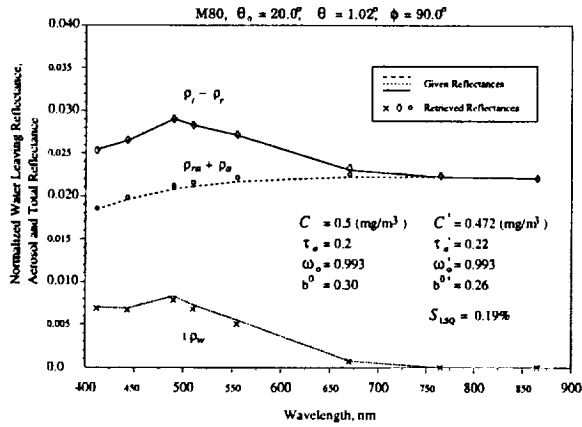
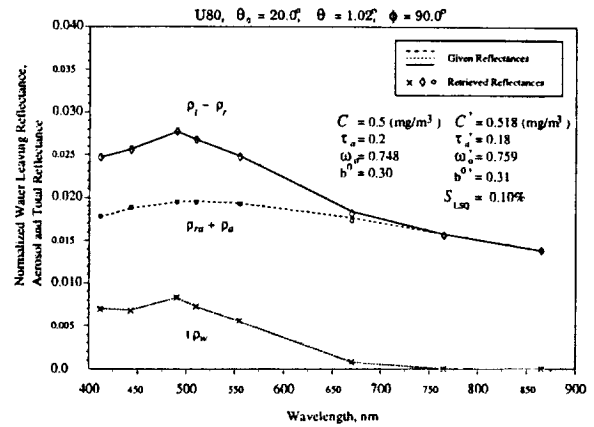


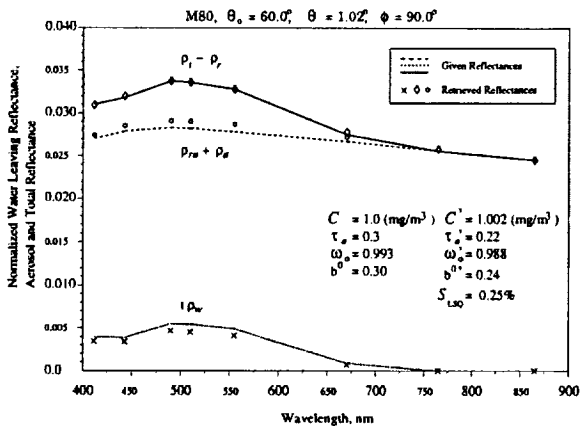
Figure 3. Comparison between the volume size distribution of the aerosol models used to generate the test pseudodata (solid curves) and the Junge power-law distribution (dotted curves).



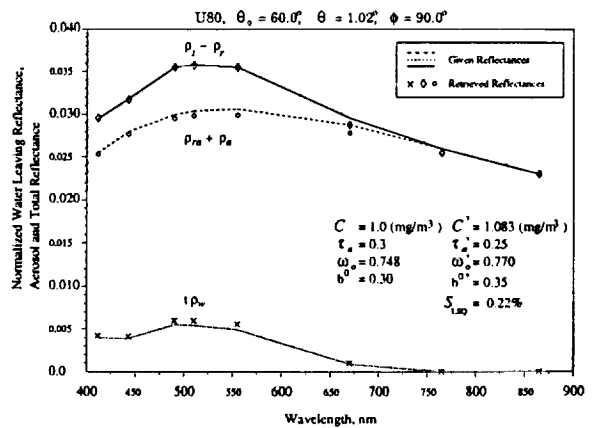
(a)



(b)

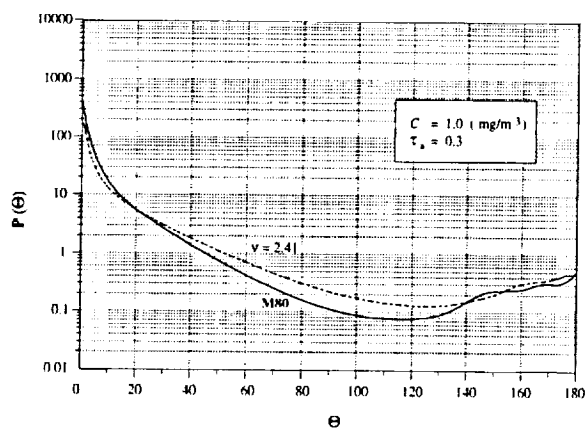


(c)

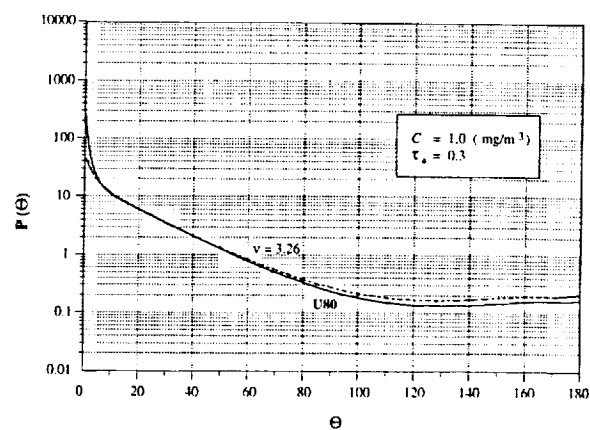


(d)

Figure 4. Comparison between the given (curves) and the retrieved (symbols) reflectances using the Junge power-law size distribution for $\theta = 1.02^\circ$ (i.e., near nadir): (a) M80 with $\theta_0 = 20^\circ$, (b) U80 with $\theta_0 = 20^\circ$, (c) M80 with $\theta_0 = 60^\circ$, (d) U80 with $\theta_0 = 60^\circ$. Unprimed parameters are the true values, primed parameters are the retrieved values.

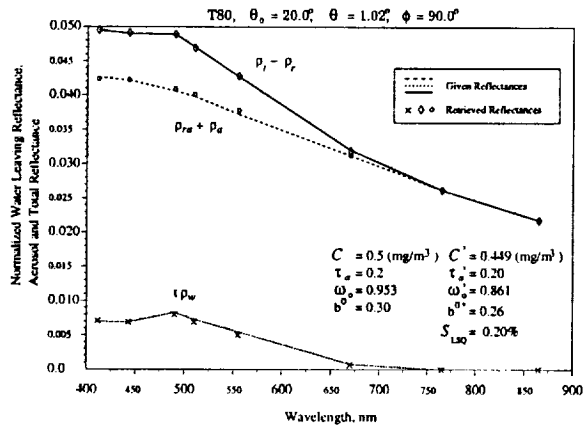


(a)

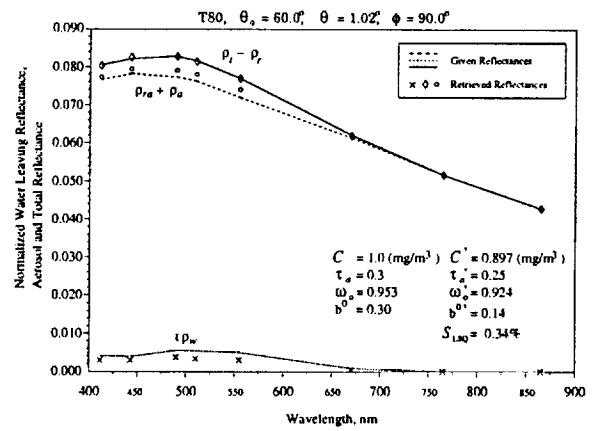


(b)

Figure 5. Comparison of the true (solid curve) and retrieved (dashed curve) phase functions at 865 nm. The retrieved phase function is used to derived the aerosol optical thickness in Figures 4c and 4d: (a) M80, (b) U80.

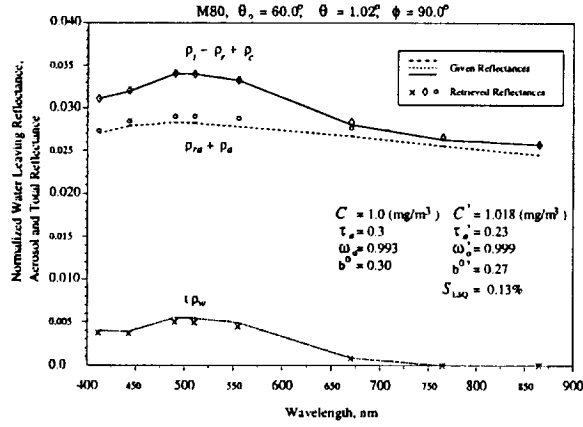


(a)

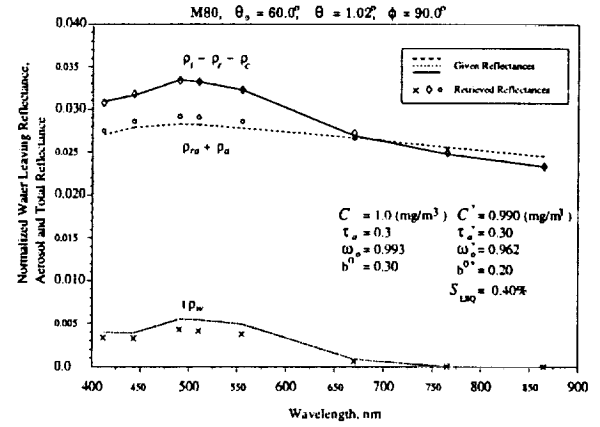


(b)

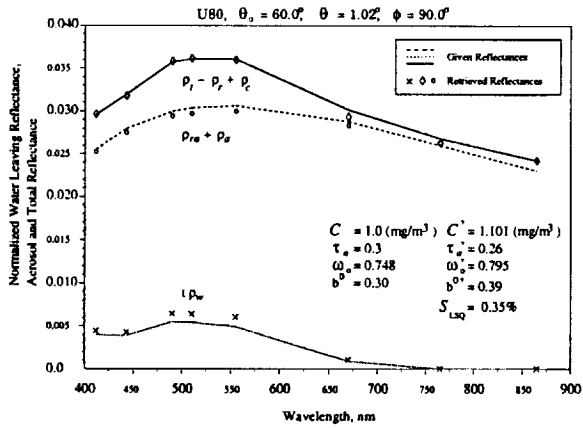
Figure 6. Comparison between the given (curves) and the retrieved (symbols) reflectances using the Junge power-law size distribution for $\theta = 1.02^\circ$ (i.e., near nadir): (a) T80 with $\theta_0 = 20^\circ$, (b) T80 with $\theta_0 = 60^\circ$. Unprimed parameters are the true values, primed parameters are the retrieved values.



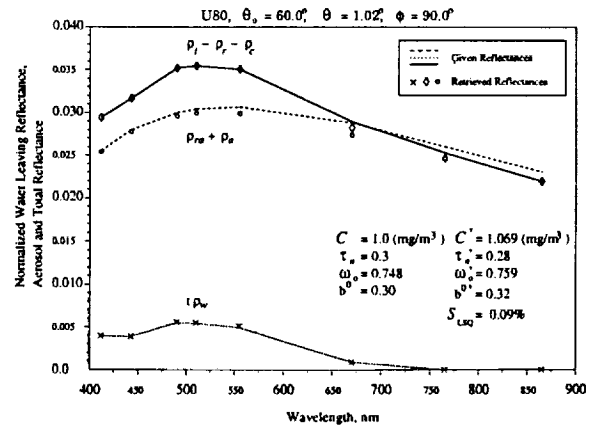
(a)



(b)

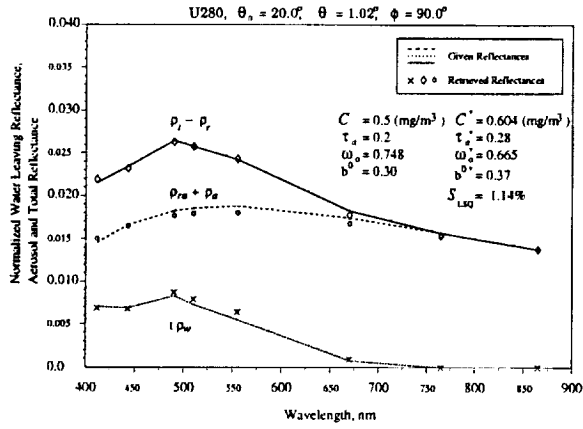


(c)

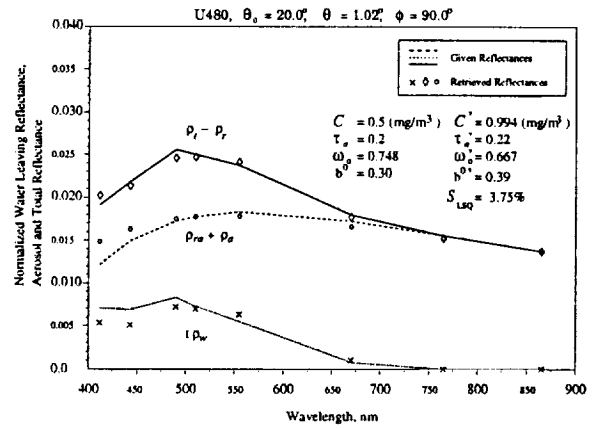


(d)

Figure 7. Comparison between the given (curves) and the retrieved (symbols) reflectances using the Junge power-law size distribution for $\theta = 1.02^\circ$ (i.e., near nadir) in the presence of the calibration errors in Table 6: (a) M80 with $\theta_0 = 60^\circ$ and positive calibration error, (b) M80 with $\theta_0 = 60^\circ$, and negative calibration error, (c) U80 with $\theta_0 = 60^\circ$ and positive calibration error, (d) U80 with $\theta_0 = 60^\circ$, and negative calibration error. Unprimed parameters are the true values, primed parameters are the retrieved values, and ρ_c represents the calibration error.



(a)



(b)

Figure 8. Comparison between the given (curves) and the retrieved (symbols) reflectances using the Junge power-law size distribution for $\theta_0 = 20^\circ$ and $\theta = 1.02^\circ$ (i.e., near nadir) for cases in which the aerosol is uniformly mixed with air from the surface to an altitude h : (a) U80 aerosol with $h = 2$ km (U280), (b) U80 aerosol with $h = 4$ km (U480). Unprimed parameters are the true values, primed parameters are the retrieved values.

Table 1: Characteristics of the test aerosol models used in the study.

Aerosol Model	Size Distribution			Refractive Index	
	N_i	D_i	σ_i	412 nm	865 nm
M80	0.990000	0.06548	0.35	$1.446 - i3.309E-3$	$1.436 - i6.107E-3$
	0.010000	0.63600	0.40	$1.359 - i5.165E-9$	$1.348 - i1.381E-6$
C80	0.995000	0.06548	0.35	$1.446 - i3.309E-3$	$1.436 - i6.107E-3$
	0.005000	0.63600	0.40	$1.359 - i5.165E-9$	$1.348 - i1.381E-6$
T80	1.000000	0.06548	0.35	$1.446 - i3.309E-3$	$1.436 - i6.107E-3$
U80	0.999875	0.07028	0.35	$1.423 - i3.473E-2$	$1.414 - i3.412E-2$
	0.000125	1.16200	0.40	$1.415 - i3.151E-2$	$1.406 - i3.095E-2$

Table 2: Values of single scattering albedo at $\lambda = 412$ and 865 nm for the test aerosol models used in the study.

Aerosol Model	λ (nm)	ω_0
M80	412	0.9923870
	865	0.9934230
C80	412	0.9883920
	865	0.9884390
T80	412	0.9758390
	865	0.9528370
U80	412	0.7823030
	865	0.7480590

Table 3

RETRIEVAL OF AEROSOL'S SINGLE-SCATTERING ALBEDO

Tabulated are mean values of retrieved ω_0 for seven Sun-Viewing Geometries and each of four hypothetical atmospheric aerosols (M80, C80, T80, U80). Also, provided are the standard deviations over viewing geometries divided by the mean (S_d) as well as the deviations from given parameters (D).

	C: mg/m ³	0.100			0.500			1.000		
		result	S_d	D	result	S_d	D	result	S_d	D
M80 $\omega_0 = 0.993$	$\tau_a(865) = 0.10$	0.938	2.5%	5.50%	0.968	1.9%	2.40%	0.972	2.2%	2.12%
	$\tau_a(865) = 0.20$	0.954	2.2%	3.93%	0.971	2.4%	2.22%	0.974	2.5%	1.91%
	$\tau_a(865) = 0.30$	0.963	1.8%	3.02%	0.976	1.9%	1.22%	0.979	2.0%	1.41%

	C: mg/m ³	0.100			0.500			1.000		
		result	S_d	D	result	S_d	D	result	S_d	D
C80 $\omega_0 = 0.988$	$\tau_a(865) = 0.10$	0.943	2.3%	4.56%	0.970	1.7%	3.20%	0.972	1.7%	1.62%
	$\tau_a(865) = 0.20$	0.960	2.1%	2.83%	0.977	1.7%	1.11%	0.979	1.8%	0.91%
	$\tau_a(865) = 0.30$	0.969	1.9%	1.92%	0.981	1.6%	0.71%	0.983	1.5%	0.51%

	C: mg/m ³	0.100			0.500			1.000		
		result	S_d	D	result	S_d	D	result	S_d	D
T80 $\omega_0 = 0.953$	$\tau_a(865) = 0.10$	0.842	4.9%	11.6%	0.867	4.5%	9.02%	0.872	4.4%	8.50%
	$\tau_a(865) = 0.20$	0.877	1.9%	8.00%	0.891	2.0%	6.51%	0.892	1.9%	6.40%
	$\tau_a(865) = 0.30$	0.902	1.6%	5.35%	0.914	1.0%	4.09%	0.918	1.0%	3.67%

	C: mg/m ³	0.100			0.500			1.000		
		result	S_d	D	result	S_d	D	result	S_d	D
U80 $\omega_0 = 0.748$	$\tau_a(865) = 0.10$	0.744	4.7%	0.54%	0.745	4.3%	1.40%	0.745	4.4%	0.40%
	$\tau_a(865) = 0.20$	0.770	0.8%	2.94%	0.769	0.8%	2.81%	0.770	1.3%	2.94%
	$\tau_a(865) = 0.30$	0.788	1.7%	5.35%	0.777	1.2%	3.88%	0.773	1.5%	3.34%

Table 4

RETRIEVAL OF OCEAN'S PIGMENT CONCENTRATION

Tabulated are mean values of retrieved C for seven Sun-Viewing Geometries and each of four hypothetical atmospheric aerosols (M80, C80, T80, U80). Also, provided are the standard deviations over viewing geometries divided by the mean (S_d) as well as the deviations from given parameters (D).

	C: mg/m ³	0.100			0.500			1.000		
		result	S_d	D	result	S_d	D	result	S_d	D
M80 $\omega_0 = 0.993$	$\tau_a(865) = 0.10$	0.096	1.8%	4.00%	0.488	1.8%	2.40%	1.012	1.1%	1.20%
	$\tau_a(865) = 0.20$	0.094	2.9%	6.00%	0.479	3.7%	4.20%	1.014	2.3%	1.40%
	$\tau_a(865) = 0.30$	0.093	3.2%	7.00%	0.473	4.6%	5.40%	1.010	3.5%	1.00%

	C: mg/m ³	0.100			0.500			1.000		
		result	S_d	D	result	S_d	D	result	S_d	D
C80 $\omega_0 = 0.988$	$\tau_a(865) = 0.10$	0.096	2.1%	4.00%	0.484	2.1%	3.20%	1.001	1.9%	0.10%
	$\tau_a(865) = 0.20$	0.094	3.2%	6.00%	0.469	1.7%	6.20%	0.984	4.3%	1.60%
	$\tau_a(865) = 0.30$	0.093	2.8%	7.00%	0.459	4.9%	8.20%	0.959	7.3%	4.10%

	C: mg/m ³	0.100			0.500			1.000		
		result	S_d	D	result	S_d	D	result	S_d	D
T80 $\omega_0 = 0.953$	$\tau_a(865) = 0.10$	0.091	4.9%	9.00%	0.466	4.0%	6.80%	1.021	6.1%	2.10%
	$\tau_a(865) = 0.20$	0.086	1.9%	14.0%	0.425	9.9%	15.0%	0.941	7.0%	5.90%
	$\tau_a(865) = 0.30$	0.090	5.7%	10.0%	0.412	6.8%	17.6%	0.874	6.7%	12.6%

	C: mg/m ³	0.100			0.500			1.000		
		result	S_d	D	result	S_d	D	result	S_d	D
U80 $\omega_0 = 0.748$	$\tau_a(865) = 0.10$	0.100	0.8%	0.00%	0.507	0.7%	1.40%	1.028	1.9%	2.80%
	$\tau_a(865) = 0.20$	0.104	1.4%	4.00%	0.526	2.7%	5.20%	1.053	3.2%	5.30%
	$\tau_a(865) = 0.30$	0.110	4.3%	10.0%	0.552	5.8%	10.4%	1.070	4.0%	7.00%

Table 5

RETRIEVAL OF WATER SCATTERING PARAMETER

Tabulated are mean values of retrieved b^0 for seven Sun-Viewing Geometries and each of four hypothetical atmospheric aerosols (M80, C80, T80, U80). Also, provided are the standard deviations over viewing geometries divided by the mean (S_d) as well as the deviations from given parameters (D).

	C: mg/m ³	0.100			0.500			1.000		
		result	S_d	D	result	S_d	D	result	S_d	D
M80 $\omega_0 = 0.993$	$\tau_a(865) = 0.10$	0.294	1.1%	2.00%	0.274	4.1%	8.67%	0.273	4.4%	3.20%
	$\tau_a(865) = 0.20$	0.289	1.7%	3.67%	0.258	7.3%	14.%	0.255	8.2%	15.0%
	$\tau_a(865) = 0.30$	0.286	1.8%	4.67%	0.249	8.2%	17.0%	0.246	9.4%	18.0%

	C: mg/m ³	0.100			0.500			1.000		
		result	S_d	D	result	S_d	D	result	S_d	D
C80 $\omega_0 = 0.988$	$\tau_a(865) = 0.10$	0.293	1.6%	2.33%	0.273	4.9%	3.20%	0.271	5.3%	9.67%
	$\tau_a(865) = 0.20$	0.289	2.2%	3.67%	0.255	8.0%	15.0%	0.250	9.0%	16.7%
	$\tau_a(865) = 0.30$	0.287	2.0%	4.33%	0.247	7.4%	17.7%	0.239	8.7%	20.3%

	C: mg/m ³	0.100			0.500			1.000		
		result	S_d	D	result	S_d	D	result	S_d	D
T80 $\omega_0 = 0.953$	$\tau_a(865) = 0.10$	0.278	6.5%	7.33%	0.237	18.%	21.0%	0.234	19.%	22.%
	$\tau_a(865) = 0.20$	0.270	6.4%	10.0%	0.200	23.%	33.3%	0.193	23.7%	36.%
	$\tau_a(865) = 0.30$	0.288	5.1%	4.00%	0.201	20.%	33.0%	0.186	25.%	38.0%

	C: mg/m ³	0.100			0.500			1.000		
		result	S_d	D	result	S_d	D	result	S_d	D
U80 $\omega_0 = 0.748$	$\tau_a(865) = 0.10$	0.297	1.0%	1.00%	0.298	1.8%	0.67%	0.298	1.7%	0.67%
	$\tau_a(865) = 0.20$	0.302	0.5%	0.67%	0.316	1.9%	5.33%	0.319	2.4%	6.33%
	$\tau_a(865) = 0.30$	0.311	1.5%	3.67%	0.350	8.2%	16.7%	0.354	8.1%	18.0%

Table 6: Mean S_{LSQ} and its standard deviation σ_S (both in %),
over all values of $\tau_a(865)$, C , and sun-viewing geometries.

Model	$\overline{S_{LSQ}}$	σ_S
M80	0.27	22
C80	0.28	19
T80	0.36	23
U80	0.15	16
U280	1.57	27
U480	5.58	27
UU80	133.48	68

Table 7: Values of the residual radiometric calibration uncertainty after effecting an in-orbit calibration adjustment.²⁸

λ_i (nm)	% Uncertainty
412	0.3
443	0.5
490	0.8
520	1.0
550	1.5
670	2.0
765	3.0
865	5.0

Table 8

RETRIEVAL OF OCEAN'S PIGMENT CONCENTRATION
with negative calibration error

Tabulated are mean values of retrieved C for seven Sun-Viewing Geometries and each of four hypothetical atmospheric aerosols (M80, C80, T80, U80). Also, provided are the standard deviations over viewing geometries divided by the mean (S_d) as well as the deviations from given parameters (D).

	C: mg/m ³	0.100			0.500			1.000		
		result	S_d	D	result	S_d	D	result	S_d	D
M80 $\omega_0 = 0.993$	$\tau_a(865) = 0.10$	0.094	2.3%	6.00%	0.479	2.3%	4.20%	1.004	0.8%	0.40%
	$\tau_a(865) = 0.20$	0.091	4.0%	9.00%	0.463	4.6%	7.40%	1.005	2.2%	0.50%
	$\tau_a(865) = 0.30$	0.090	4.7%	3.00%	0.452	6.1%	9.60%	0.998	4.0%	0.20%

	C: mg/m ³	0.100			0.500			1.000		
		result	S_d	D	result	S_d	D	result	S_d	D
C80 $\omega_0 = 0.988$	$\tau_a(865) = 0.10$	0.094	2.6%	6.00%	0.476	2.5%	4.80%	0.997	0.9%	0.30%
	$\tau_a(865) = 0.20$	0.090	4.7%	10.0%	0.455	5.2%	9.00%	0.983	2.2%	1.70%
	$\tau_a(865) = 0.30$	0.088	5.3%	12.0%	0.438	6.5%	12.4%	0.964	4.4%	3.60%

	C: mg/m ³	0.100			0.500			1.000		
		result	S_d	D	result	S_d	D	result	S_d	D
T80 $\omega_0 = 0.953$	$\tau_a(865) = 0.10$	0.086	10.%	5.00%	0.437	9.5%	12.6%	1.038	14.%	3.80%
	$\tau_a(865) = 0.20$	0.078	14.%	22.0%	0.377	19.%	24.6%	0.836	3.4%	16.4%
	$\tau_a(865) = 0.30$	0.081	12.%	19.0%	0.337	15.%	32.6%	0.640	26.%	36.0%

	C: mg/m ³	0.100			0.500			1.000		
		result	S_d	D	result	S_d	D	result	S_d	D
U80 $\omega_0 = 0.748$	$\tau_a(865) = 0.10$	0.098	1.5%	2.00%	0.496	0.2%	0.80%	1.021	2.7%	2.10%
	$\tau_a(865) = 0.20$	0.099	2.7%	1.00%	0.507	1.9%	1.40%	1.033	3.5%	3.30%
	$\tau_a(865) = 0.30$	0.104	3.2%	4.0%	0.530	4.7%	6.00%	1.056	4.1%	5.60%

Table 9

**RETRIEVAL OF OCEAN'S PIGMENT CONCENTRATION
with positive calibration error**

Tabulated are mean values of retrieved C for seven Sun-Viewing Geometries and each of four hypothetical atmospheric aerosols (M80, C80, T80, U80). Also, provided are the standard deviations over viewing geometries divided by the mean (S_d) as well as the deviations from given parameters (D).

	C: mg/m ³	0.100			0.500			1.000		
		result	S_d	D	result	S_d	D	result	S_d	D
M80 $\omega_0 = 0.993$	$\tau_a(865) = 0.10$	0.098	1.6%	2.00%	0.494	2.7%	1.20%	1.011	4.2%	1.10%
	$\tau_a(865) = 0.20$	0.097	2.2%	3.00%	0.487	5.0%	2.60%	0.999	8.5%	0.10%
	$\tau_a(865) = 0.30$	0.097	2.2%	3.00%	0.485	6.2%	3.00%	0.991	11.1%	0.90%

	C: mg/m ³	0.100			0.500			1.000		
		result	S_d	D	result	S_d	D	result	S_d	D
C80 $\omega_0 = 0.988$	$\tau_a(865) = 0.10$	0.098	1.6%	2.00%	0.490	3.6%	2.00%	0.995	6.3%	0.50%
	$\tau_a(865) = 0.20$	0.097	2.2%	3.00%	0.478	7.1%	4.40%	0.966	12.1%	3.40%
	$\tau_a(865) = 0.30$	0.097	2.6%	3.00%	0.471	10.1%	5.80%	0.940	17.1%	6.00%

	C: mg/m ³	0.100			0.500			1.000		
		result	S_d	D	result	S_d	D	result	S_d	D
T80 $\omega_0 = 0.953$	$\tau_a(865) = 0.10$	0.095	4.7%	5.00%	0.487	2.4%	2.60%	1.037	4.9%	3.70%
	$\tau_a(865) = 0.20$	0.093	1.3%	7.00%	0.470	4.0%	6.00%	0.935	3.0%	6.50%
	$\tau_a(865) = 0.30$	0.096	4.4%	4.0%	0.469	2.1%	6.20%	0.943	2.7%	5.70%

	C: mg/m ³	0.100			0.500			1.000		
		result	S_d	D	result	S_d	D	result	S_d	D
U80 $\omega_0 = 0.748$	$\tau_a(865) = 0.10$	0.103	0.8%	3.00%	0.519	1.1%	3.80%	1.043	2.3%	4.30%
	$\tau_a(865) = 0.20$	0.109	2.8%	9.00%	0.543	3.8%	8.60%	1.062	2.9%	6.20%
	$\tau_a(865) = 0.30$	0.116	5.7%	16.0%	0.573	6.4%	14.6%	1.089	3.6%	8.90%

Table 10

RETRIEVAL OF OCEAN'S PIGMENT CONCENTRATION

Tabulated are mean values of retrieved C for seven Sun-Viewing Geometries and each of four hypothetical atmospheric aerosols (M80, C80, T80, U80). Also, provided are the standard deviations over viewing geometries divided by the mean (S_d) as well as the deviations from given parameters (D).

	$C: \text{mg/m}^3$	0.100			0.500			1.000		
		result	S_d	D	result	S_d	D	result	S_d	D
U80 $\omega_0 = 0.748$	$\tau_a(865) = 0.10$	0.100	0.8%	0.00%	0.507	0.7%	1.40%	1.028	1.9%	2.80%
	$\tau_a(865) = 0.20$	0.104	1.4%	4.00%	0.526	2.7%	5.20%	1.053	3.2%	5.30%
	$\tau_a(865) = 0.30$	0.110	4.3%	10.0%	0.552	5.8%	10.4%	1.070	4.0%	7.00%

	$C: \text{mg/m}^3$	0.100			0.500			1.000		
		result	S_d	D	result	S_d	D	result	S_d	D
U280 $\omega_0 = 0.748$	$\tau_a(865) = 0.10$	0.110	2.8%	10.0%	0.602	9.8%	20.4%	1.305	11.1%	30.5%
	$\tau_a(865) = 0.20$	0.122	6.3%	22.0%	0.575	3.0%	15.0%	1.120	7.9%	12.0%
	$\tau_a(865) = 0.30$	0.138	12.1%	38.0%	0.631	16.1%	26.2%	0.959	8.6%	4.10%

	$C: \text{mg/m}^3$	0.100			0.500			1.000		
		result	S_d	D	result	S_d	D	result	S_d	D
U480 $\omega_0 = 0.748$	$\tau_a(865) = 0.10$	0.120	6.7%	20.0%	0.941	28.1%	88.2%	1.500	0.0%	50.0%
	$\tau_a(865) = 0.20$	0.142	14.1%	42.0%	1.198	19.1%	140.1%	1.500	0.0%	50.0%
	$\tau_a(865) = 0.30$	0.172	25.1%	72.0%	1.084	13.1%	102.1%	1.500	0.0%	50.0%